



## ABSTRACT

Title of Thesis: Calibration and Performance Studies of the Coordinate Detector for the Super BigBite Spectrometer in Jefferson Lab's Hall A via Geant4 Simulation and ROOT Analysis

Degree candidate: Lydia Ellen Lorenti

Degree and Year: Master of Science, 2019

Thesis directed by: Edward Brash, Ph.D., Professor, Department of Physics, Computer Science and Engineering

A new spectrometer is being built for Hall A at Jefferson Lab (JLab) at 12 GeV. One of its detectors is the Coordinate Detector (CDet), a multipurpose scintillator-based detector that will provide supplemental tracking in several experiments. Particles are detected by CDet as they pass through and deposit energy in the detector, ultimately resulting in digital output signals called ADC (Analog-to-Digital Converter) signals. The ADC output needed to be calibrated to the corresponding energy deposition in order to be used in particle identification. A Geant4 simulation was used along with test data taken using cosmic rays to calibrate CDet. The simulated output data was fitted to the test data, and the known energy data from the simulation was used to obtain the proportionality between energy deposition and ADC signal. The performance parameters studied were found to be highly satisfactory.

**CALIBRATION AND PERFORMANCE STUDIES OF THE COORDINATE  
DETECTOR FOR THE SUPER BIGBITE SPECTROMETER IN  
JEFFERSON LAB'S HALL A VIA GEANT4 SIMULATION  
AND ROOT ANALYSIS**

by

Lydia Ellen Lorenti

Thesis submitted to the Graduate Faculty of  
Christopher Newport University in partial  
fulfillment of the requirements  
for the degree of  
Master of Science  
2019

Approved:

Edward Brash, Chair \_\_\_\_\_

David Heddle \_\_\_\_\_

Peter Monaghan \_\_\_\_\_

ProQuest Number:22617833

All rights reserved

INFORMATION TO ALL USERS

The quality of this reproduction is dependent upon the quality of the copy submitted.

In the unlikely event that the author did not send a complete manuscript and there are missing pages, these will be noted. Also, if material had to be removed, a note will indicate the deletion.



ProQuest 22617833

Published by ProQuest LLC (2019). Copyright of the Dissertation is held by the Author.

All rights reserved.

This work is protected against unauthorized copying under Title 17, United States Code  
Microform Edition © ProQuest LLC.

ProQuest LLC.  
789 East Eisenhower Parkway  
P.O. Box 1346  
Ann Arbor, MI 48106 – 1346

Copyright by Lydia Ellen Lorenti 2019

All Rights Reserved

## ACKNOWLEDGEMENTS

First, I would like to thank my advisor, Dr. Edward Brash, for his guidance, mentorship, and support. He was exactly the advisor I needed, and this would not have been possible without him. I would like to thank the other members of my committee, Dr. David Heddle and Dr. Peter Monaghan, for their mentorship and support as well. I cannot imagine a better thesis committee than these three. Finally, I would like to thank my mom for her constant support and encouragement during this project.

# TABLE OF CONTENTS

Section	Page
List of Tables	v
List of Figures	vi
Chapter I Introduction	
Electron scattering as a probe of nucleon structure	1
Jefferson Lab and CEBAF	2
Hall A at Jefferson Lab	3
The Super BigBite Spectrometer	3
The Coordinate Detector with SBS	5
Detector simulations as a means of characterizing detector performance	7
Geant4 – An overview	8
Outline of thesis work	9
Chapter II The Coordinate Detector	
Design and construction details	10
Scintillator background and key design properties	14
WLS background and key design properties	15
MAPMT background and key design properties	15
Expected detector performance parameters	17
Test setup at JLab	19
Description of test data	20
Chapter III Geant4 Simulation	
Design of CDet simulation	22
Detector model design overview	22
Detector construction	23
Material properties	26
Primary generation	29
ROOT	30
Generation of cosmic muons	30
Physics processes	33
Detection	34
Hits and hit processing	35
Resulting simulation data	37
Chapter IV Analysis	
Analysis background	39
Test data analysis code and vertical track selection	39
Simulation data analysis code	42
Testing of optical efficiency	46

Calibration of ADC spectra	52
General procedure	53
Initial testing	54
Major modifications and troubleshooting	54
Final analysis and results	59
Crosstalk analysis	70
Detection efficiency and experimental threshold	75
Chapter V Conclusions	
References	79



## LIST OF TABLES

Number		Page
1.	Summary, by category, of simulation data recorded from each primary event	38
2.	Final ADC calibration analysis parameters	66

## LIST OF FIGURES

Number	Page
1. The CEBAF accelerator [4]	3
2. SBS proton experiment schematic [9]	4
3. SBS neutron experiment schematic [9]	5
4. Chain of proportionality between all signals in scintillator detector	6
5. Diagram of one CDet module (front view)	10
6. Diagram of one CDet scintillator bar	10
7. Diagram of one CDet scintillator paddle with WLS fiber	11
8. 3-D diagram of WLS fibers connecting from paddles to coupler [9]. Module is laid flat in this drawing.	12
9. The 16 pixels on the maPMT are arranged in a $4 \times 4$ matrix, so the coupler spaces the WLS fibers accordingly. LEFT: Diagram of coupler holding 16 WLS fibers in the proper arrangement. RIGHT: Diagram of maPMT with 16 pixels.	12
10. Diagram of scintillator bar staggering in one layer of CDet for detector acceptance matching. The general curvature of the scintillator stacks follows the right side of a circle.	13
11. Diagram of paddle tilting in CDet layer. Red line is center of layer vertically. [17]	14
12. Example map of maPMT pixels and connected paddle fibers	17
13. Estimate of detection efficiency as a function of energy threshold [16]	18
14. Side view cross section diagram of module test setup	19
15. Photograph of module test setup at JLab	20
16. Top view diagram of simulated CDet bar	23

17.	3-D visualization of Geant4 CDet bar model. Red line poking through center of setup represents a single primary muon track. The green lines represent photon tracks emerging from the uncovered ends of the scintillator paddles.	26
18.	Distribution of scintillation wavelengths (in nanometers)	28
19.	Distribution of WLS fiber reemission wavelengths (in nm)	28
20.	Momentum distribution for cosmic muons	31
21.	Example of vertical track ADC distribution for one paddle. The $x$ -axis shows the ADC channel spectrum, and the $y$ -axis shows histogram counts. Black curves are Gaussian fits.	41
22.	Raw photoelectron number distribution for one paddle/PMT in the simulation	44
23.	Raw distribution of energy deposition in one paddle in the simulation	45
24.	Plot of energy deposition vs. number of photoelectrons per primary event, per paddle. Energy deposition is on the $y$ -axis in units of MeV; number of photoelectrons produced is on the $x$ -axis.	46
25.	Side-view diagram of bar model showing the five incident primary regions along the bar length used in the five simulation runs. Incident primary regions are indicated by red separating lines. Center coordinate of each region is labeled on the $x$ -axis.	47
26.	3D visualization of bar model, with end mirror on. Green lines represent photon tracks; red lines represent primary muon tracks.	48
27.	3D visualization of bar model, end mirror removed. Notice the spray of photons (green lines) out the back end of the bar.	48
28.	Mean photoelectron yield vs. center position of incident primary region over length of bar. Photoelectron yield values are represented as fractions of the maximum value in each graph. Error bars are inside data points.	49
29.	Mean photoelectron yield vs. center position of incident primary region over length of bar. Yield values are represented as fractions of the maximum yield occurring with the mirror on. Error bars are inside data points.	50

30.	Ratio of photoelectron yield, mirror-on to mirror-off, vs. center position of incident primary region over length of bar. Error bars are inside data points. The lowest value shown on the $y$ -axis is 1, not 0.	51
31.	Diagram of trigger paddle geometry in CDet test setup	57
32.	Distribution of primary $\theta$ without cut	58
33.	Distribution of primary $\theta$ without cut for non-pedestal events	59
34.	Profile of energy deposition vs. photoelectron number 2D histogram, with linear fit.	60
35.	Energy deposition distribution of near-vertical primary muons in one paddle. The polar angle $\theta$ is restricted to the range $3.05 \leq \theta \leq \pi$ .	61
36.	Overlaid distributions of photoelectron number from test data and simulation for one paddle. Dark blue curves are Gaussian fits to the peaks in the test data. Dark red curves are Gaussian fits to the peaks in the simulated data.	63
37.	Photoelectron number distribution plots for all paddles analyzed. Blue curves are Gaussian fits on test data peaks (blue histograms); red curves are Gaussian fits on simulated data peaks (red histograms). Axes are the same as in Fig. 36.	64
38.	Distributions of photoelectron number in the outer two paddles of the bar, when the neighbor cut is only applied to one neighboring paddle and not two.	65
39.	Resolutions of the fits on the vertical track peaks in the photoelectron number distributions.	67
40.	Approximate data counts in the vertical track peaks in the photoelectron number distributions	68
41.	Map of maPMT pixels and connected paddle fibers for PMT 7 in CDet Module 1, right half	71
42.	2-D histogram showing PE signal in one pixel vs. PE signal in adjacent pixel with non-adjacent paddle for test data. Signal values along $x$ -axis are all above the pedestal. Data counts are shown by color scale.	73
43.	2-D histogram showing PE signal in one paddle vs. PE signal in non-adjacent paddle for simulated data. Signal values along $x$ -axis are all above the pedestal. Data counts are shown by color scale.	73

- 44. 2-D histogram showing PE signal in one pixel vs. PE signal in adjacent pixel with adjacent paddle for test data. Signal values along  $x$ -axis are all above the pedestal. Data counts are shown by color scale. 74
- 45. 2-D histogram showing PE signal in one paddle vs. PE signal in adjacent paddle for simulated data. Signal values along  $x$ -axis are all above the pedestal. Data counts are shown by color scale. 74

# CHAPTER I:

## INTRODUCTION

### Electron scattering as a probe of nucleon structure

In nuclear and particle physics, a primary subject of interest is the structure of nucleons (protons and neutrons). One of the principal methods to study nucleon structure is to scatter a beam of probe particles off target nuclei and observe the results of the interaction. Electrons are ideal scattering probes for this purpose. Electrons, according to current knowledge, are point particles, so they have no structure of their own to introduce complications into the interpretation of the data [1]. They interact via the electromagnetic interaction, which is described by the theory of quantum electrodynamics (QED). Processes in QED can be calculated to high precision because the electromagnetic coupling constant is small, i.e.  $\alpha \ll 1$ , so perturbation theory holds [2]. Both QED and the behavior of point particles are well understood. Thus, in the study of nucleon structure, electron scattering uses what is well known to probe what is not well known [1]. Also, nucleon structure arises from the strong interaction between quarks, but electrons do not interact strongly. Therefore, electrons will not interfere with the source of the structure being studied. Additionally, a practical advantage is that electrons are common, stable particles. With current technology, it is relatively easy to manipulate electron beams, control their energy, and detect individual electrons after scattering [2].

Electrons, being electrically charged particles, probe the charge distribution of nucleons. The charged particles inside nucleons are the quarks. Thus electrons can also probe the quark distributions of nucleons. The choice of electron energy determines the distance scale at which the target structure is probed. The energy determines the momentum, which determines the de Broglie wavelength of the electron. The distance scale probed is on the same order of magnitude as the de Broglie wavelength [1].

Different modes of scattering probe different distance scales. For example, elastic scattering occurs when the de Broglie wavelength  $\lambda$  of the electron is greater than the size of the nucleon. In this case, the electron tends to interact with the nucleon as a whole, probing its overall charge and density distribution [2]. Another mode, deep inelastic scattering, occurs when  $\lambda$  is less than the nucleon size. Here, the electron interacts with an individual quark inside the nucleon, knocking it out and producing hadronic fragments. In this case, the quark distribution in the nucleon is probed [2].

### **Jefferson Lab and CEBAF**

Jefferson Lab (JLab) is a facility dedicated to studying the structure and properties of nucleons (and nuclei) using electron scattering [3]. It is home to the Continuous Electron Beam Accelerator Facility (CEBAF). CEBAF is a racetrack-shaped accelerator with a maximum beam energy of 12 GeV (a recent upgrade from the former 6 GeV). A 12 GeV electron beam has a de Broglie wavelength of about 0.1 femtometers (fm), while the radius of a nucleon is about 1 fm, making the CEBAF beam ideal for probing internal nucleon structure. CEBAF is connected to four underground experimental halls, termed A, B, C, and D. Each hall houses a target and a large detector setup. Different halls are designed for different types of experiments. A diagram of CEBAF, with some of the 12 GeV upgrades labeled, is shown in Fig. 1.

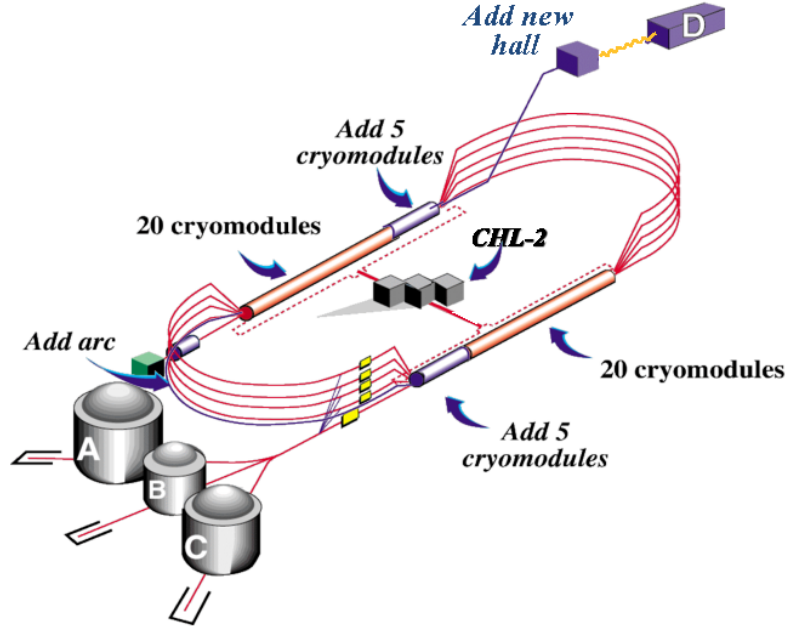


Figure 1: The CEBAF accelerator [4]

### *Hall A at Jefferson Lab*

Hall A [5] is the largest hall at JLab. It is designed for high-precision experiments. Its size allows it to house large magnetic spectrometers, which are necessary to achieve high resolution. Its experiments also use a high-power cryotarget. The detector equipment in Hall A is being upgraded for use with the 12 GeV beam. Three brand new spectrometers are being built for Hall A at 12 GeV, one of which is the Super BigBite Spectrometer [5].

### *The Super BigBite Spectrometer*

Unlike most spectrometers, the Super BigBite Spectrometer (SBS) [6] is modular and can be rearranged for different experiments [7]. It is a high-resolution spectrometer with a large acceptance [8]. SBS is designed for an experimental program that will use



the new 12 GeV beam to explore elastic scattering at high- $Q^2$ , a region in which most processes are deep inelastic scattering. This means the rates for elastic scattering are very low, so the large acceptance is required in order to increase the number of detected events [8]. One of the main experimental goals for SBS is to measure the electric and magnetic form factors of the proton and neutron [7].

SBS has two detector arms. One arm detects hadrons, and the other detects electrons [7]. There are two main configurations of the arms: one for experiments which will detect scattered protons, and one for experiments which will detect scattered neutrons [7, 9].

***Proton form factors ratio, GEp(5): E12-07-109***

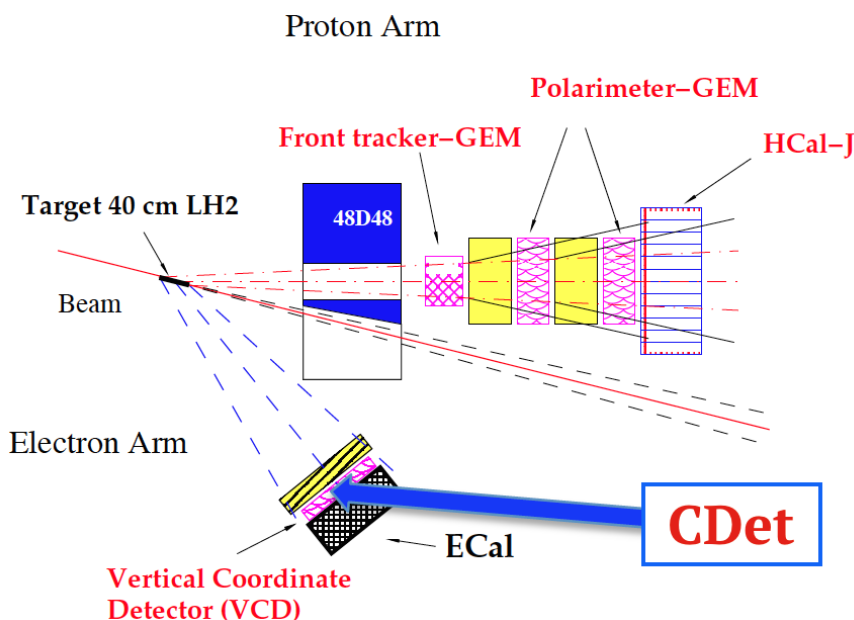


Figure 2: SBS proton experiment schematic [9]

### Neutron experiment: GMn/GMp E12-09-019

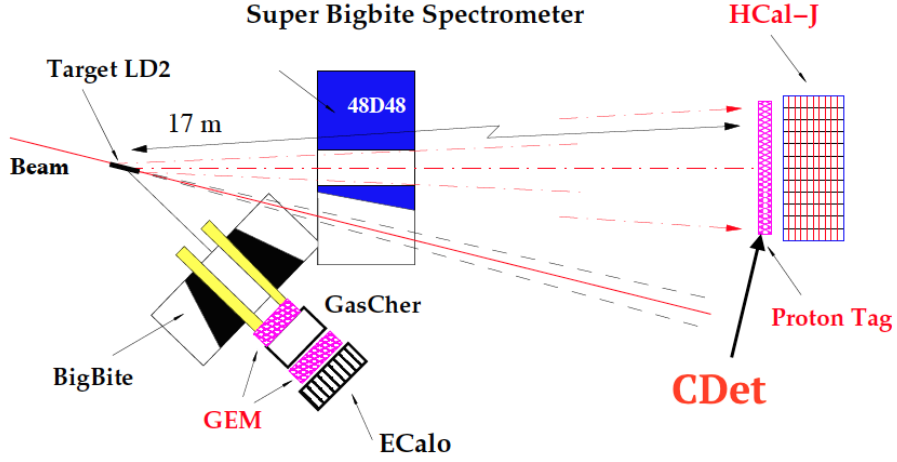


Figure 3: SBS neutron experiment schematic [9]

In both configurations, there is a large dipole magnet at the front of the hadron arm and a hadron calorimeter at the end of the hadron arm. There is an electromagnetic calorimeter at the end of the electron arm. In the proton configuration (shown in Fig. 2), a tracker and polarimeter setup is placed between the magnet and the hadron calorimeter. A supplemental coordinate detector (CDet) is placed in front of the electromagnetic calorimeter. In the neutron configuration (shown in Fig. 3), only the coordinate detector is placed in front of the hadron calorimeter. On the electron arm, the smaller BigBite spectrometer is placed in front of the electromagnetic calorimeter along with additional trackers [7, 9].

#### *The Coordinate Detector with SBS*

The coordinate detector (CDet) [10] is a multipurpose scintillator-based detector. In proton experiments, it serves as a supplemental tracking detector for charged particles (electrons). It is constructed with stacks of narrow plastic scintillator paddles to detect the vertical coordinate of a scattered particle. The vertical position then

provides the out-of-plane angle of the particle's trajectory. In neutron experiments, CDet serves as a charged particle veto to distinguish neutrons from other, charged particles.

A scintillator produces light due to the ionization and reabsorption of electrons when a charged particle passes through it. In a scintillator detector, the light is collected by photodetectors. In CDet, the photodetectors are photomultiplier tubes (PMTs). A PMT amplifies a photon signal via the photoelectric effect along with secondary electron emission [11], producing an electronic current signal. The current signal is then integrated, and the resultant integrated charge is converted into a corresponding digital value by an analog-to-digital converter (ADC). These digital values are known as ADC channels. Proportionality is assumed to hold for all of the signal conversions throughout the entire detection process, as shown in Fig. 4.

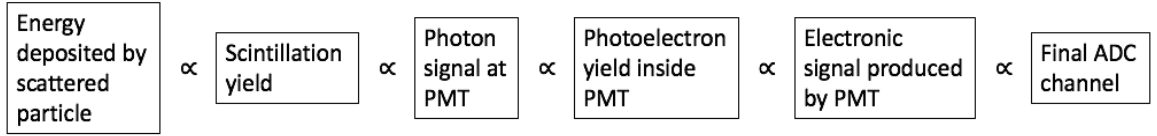


Figure 4: Chain of proportionality between all signals in scintillator detector

This means that the ADC signal should be proportional to the energy deposited in the scintillator by the scattered particle. The energy deposition can help identify the particle and is an important experimental quantity. Therefore, it is necessary to calibrate the ADC spectrum to determine the proportionality constant between ADC channel and energy deposited. CDet is currently undergoing testing with cosmic rays, but test data alone is insufficient for calibration. To calibrate the ADC spectrum, the energy deposited by each incident particle must be known.

## **Detector simulations as a means of characterizing detector performance**

An ideal solution to the above problem is to use a simulation of the coordinate detector. Simulations are an important tool in modern experimental particle physics [12, 13]. Software models are essential for designing, building, and commissioning complex particle physics detectors [13]. They are more realistic and experiment-specific than theoretical models alone. They can provide access to information that cannot be obtained from experimental data. They can allow researchers to observe internal processes within the detector, which are invisible in real experimental data, and so can be used to test internal efficiency. They can also show what good data is expected to look like [13]. Additionally, changes can be made to the simulated detector and the results tested relatively quickly without having to make any changes to the real detector.

In particle physics, an event consists of all the data resulting from a single occurrence of an experiment, e.g. a single collision, a single scattering, or a single incident particle [13]. Simulation software is designed to produce events that are identical, or nearly identical, to the events that occur in the real experiment. The data output from the simulation usually also has the same format as the experimental data, so both data sets can be processed and analyzed in the same way [13].

Simulations usually consist of a series of modules [13]. The first module is the generator. The generator produces particles to be observed in the detector, using Monte Carlo methods to reproduce experimentally measured distributions [12, 13]. The second module simulates the passage of the generated particles through the detector. This is called “Monte Carlo radiation transportation,” or sometimes just “detector simulation” [12]. It involves both in-medium physics processes and geometry boundary interactions [12]. Therefore, all detector materials, major detector geometry, and relevant physics processes must be specified in order for the simulation

to be accurate. Geometry is specified by the volumes and relative placements of the detector components. A material is assigned to each volume. Parameters are specified which describe all relevant properties of all materials, including air. Depending on the scope of the simulation, a third module might be included to simulate the detector electronics, which produce the electrical signals output by the detector [12, 13]. To accurately describe the electronic components, all relevant parameters (e.g. efficiencies) must be specified.

### **Geant4 – An overview**

Geant4 [14] is a free, highly popular simulation software package for particle physics experiments. It is a comprehensive toolkit for all aspects of the simulation, including the geometry of the detector system, the materials in the system, the particles involved, the generation of primaries, tracking of particles through materials and electromagnetic fields, physics processes, the responses of electronic components, generation of event data, storage of data, visualization of the detector system and particle trajectories, and data analysis [15]. Geant4 comes with a set of default materials that can be used when modeling the detector, but the user can also easily define their own. It also contains an extensive collection of physics models to describe particle interactions with matter over a wide range of energies, serving, in a sense, as a repository of knowledge about particle interactions [15]. Geant4 is written in C++ in an object-oriented style, making it easy to extend and customize for the particular purposes of a given experiment [15]. The user can implement and use whatever components of the software are necessary; while Geant4 provides functionality for the entire simulation process, parts of it can be used just as well in combination with other tools.

## Outline of thesis work

In order to calibrate the CDet ADC spectra, a Geant4 simulation of CDet is used. The simulated spectra are fitted to the spectra from the test data to ensure accuracy. To find the proportionality between ADC channel and primary energy deposition, two other proportionalities are used: the number of photoelectrons produced per unit of energy deposited by the primary particle, and the number of photoelectrons per ADC channel. The simulation, when proper cuts and fit parameters are included, provides the photoelectron-to-energy ratio, as well as the energy deposited by the primary particles. The simulation also provides the mean number of photoelectrons produced per primary event. This, along with the final spectra from the ADC calibration, is used to verify the detection efficiency of CDet.

Additionally, some analysis is done for the CDet PMTs. Instead of having a single PMT for each paddle, CDet uses multi-anode PMTs (maPMTs) [16]. Each maPMT is equivalent to 16 individual PMTs; each individual PMT equivalent is called a “pixel.” If a large signal is generated in one pixel, there is a possibility of charge leakage to adjacent pixels, resulting in false signals. This charge leakage is called “crosstalk.” It is important to understand the amount and behavior of crosstalk in the maPMTs in order to properly interpret the data. Therefore, the simulation is used to analyze the amount of crosstalk present in the maPMTs.

## CHAPTER II: THE COORDINATE DETECTOR

### Design and construction details

CDet consists of two layers of scintillators. Each layer is divided vertically into three modules (top, middle, bottom), and each module has separate left and right halves. Each half-module is composed of 14 stacked scintillator “bars,” where one bar is a stack of 14 scintillator paddles. Therefore, a half-module has 196 data channels (one channel per paddle), a whole module has 392 channels, and the entire detector has a total of 2352 channels.

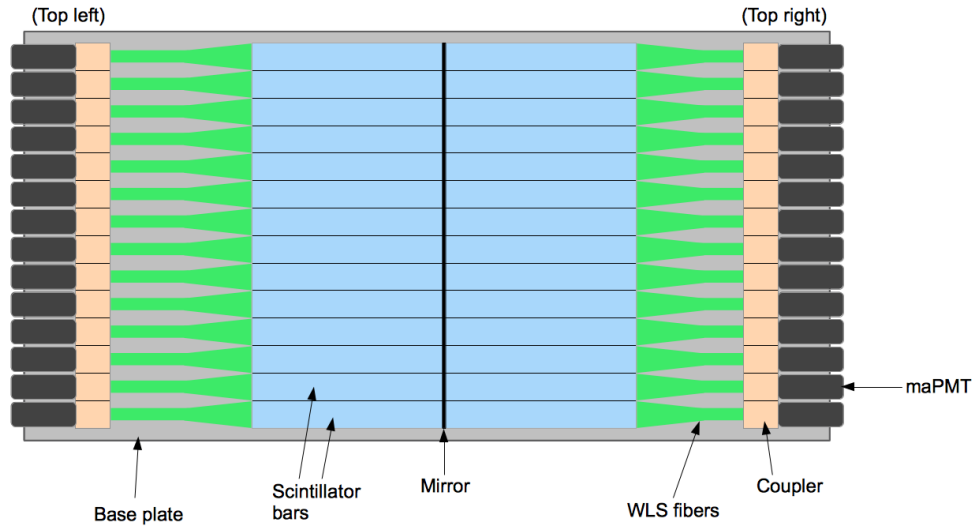


Figure 5: Diagram of one CDet module (front view)

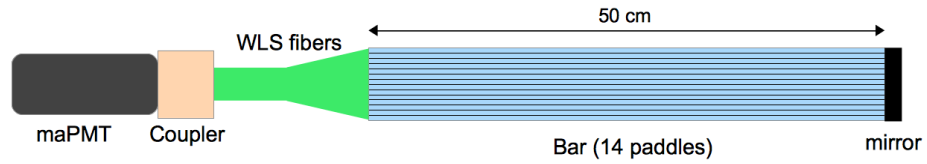


Figure 6: Diagram of one CDet scintillator bar

One scintillator paddle (see Fig. 7) measures 50 cm long  $\times$  4 cm wide  $\times$  0.5 cm thick. This means a half-module is 50 cm wide and about 100 cm tall, so each module has about 1 m<sup>2</sup> of active detector area, and each layer has about 3 m<sup>2</sup> of active detector area. Each paddle has a wavelength shifting (WLS) fiber 2 mm in diameter threaded through its full length down the center. The fibers extend out from the paddles and connect to the maPMTs. One maPMT is used for each bar, for a total of 28 maPMTs per module. Each WLS fiber connects to one pixel on the maPMT. The fibers are fed through a coupler, which holds them in place and spaces them properly, and the ends are pressed up against the PMT pixels. There are 16 fibers that connect through each coupler to each maPMT; 14 are from the scintillator bar, and the other two are redundant and unconnected to the detector.

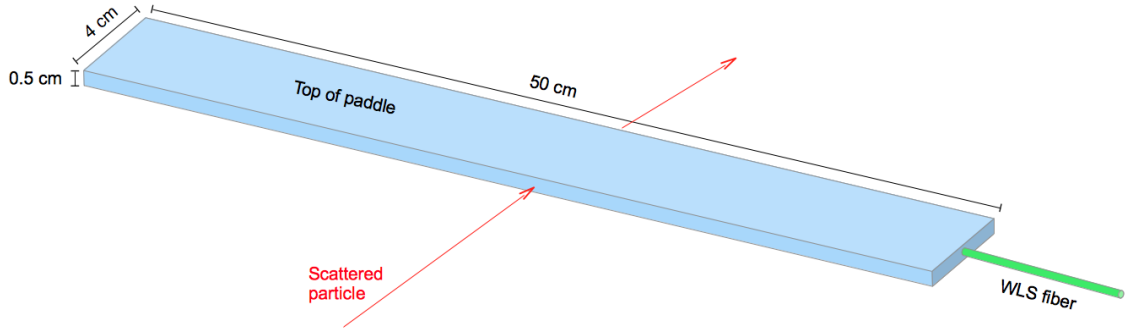


Figure 7: Diagram of one CDet scintillator paddle with WLS fiber



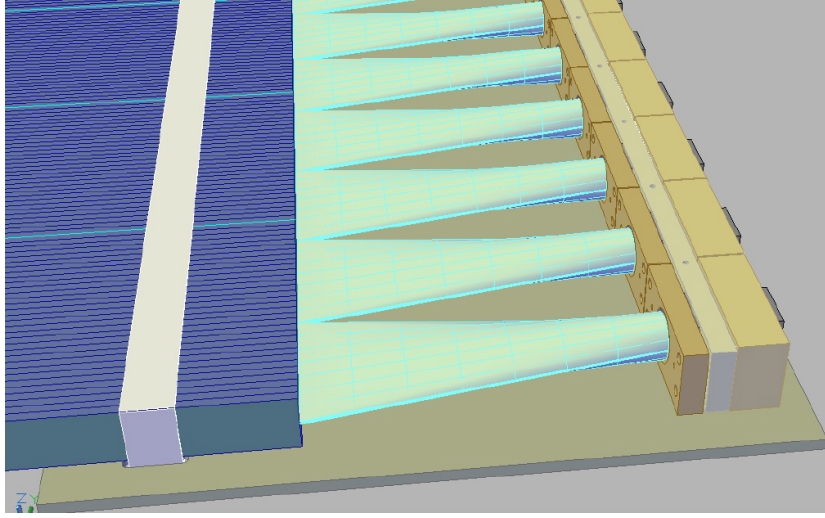
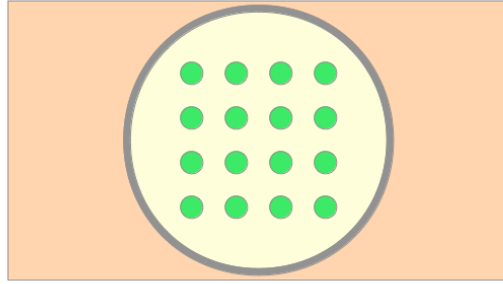
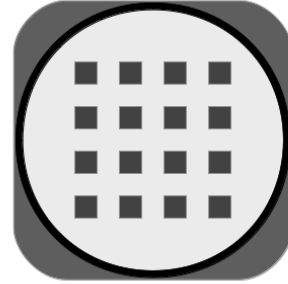


Figure 8: 3-D diagram of WLS fibers connecting from paddles to coupler [9]. Module is laid flat in this drawing.



Coupler with 16 WLS fibers



maPMT with 16 pixels

Figure 9: The 16 pixels on the maPMT are arranged in a  $4 \times 4$  matrix, so the coupler spaces the WLS fibers accordingly. LEFT: Diagram of coupler holding 16 WLS fibers in the proper arrangement. RIGHT: Diagram of maPMT with 16 pixels.

To optically isolate each paddle from other neighboring paddles and from the external environment, each paddle is wrapped in a layer of aluminized mylar. After the paddles are glued together, each bar is also wrapped in an additional layer of aluminized mylar. A mirror separates the left and right halves of each module; the inner ends of the paddles are pressed up against the mirror so that it reflects the scintillation light back into each paddle to maximize the probability of absorption by the WLS fibers, which

then carry the reemitted photons to the PMTs. Each module, including scintillator, fibers, and PMTs, is completely encased in a housing made of aluminum plates.

In each layer, the scintillator bars are arranged to match the detector acceptance to the curvature of the cone of scattered particles when CDet is used on the electron arm of SBS (Fig. 10). The individual paddles are also tilted slightly through the height of each layer (Fig. 11) so that a scattered particle will pass through the entire 4 cm width of a single paddle, regardless of the particle's out-of-plane angle. The tilt angles of the paddles are designed to meet this goal when CDet is placed in front of the electromagnetic calorimeter on the electron arm of SBS.

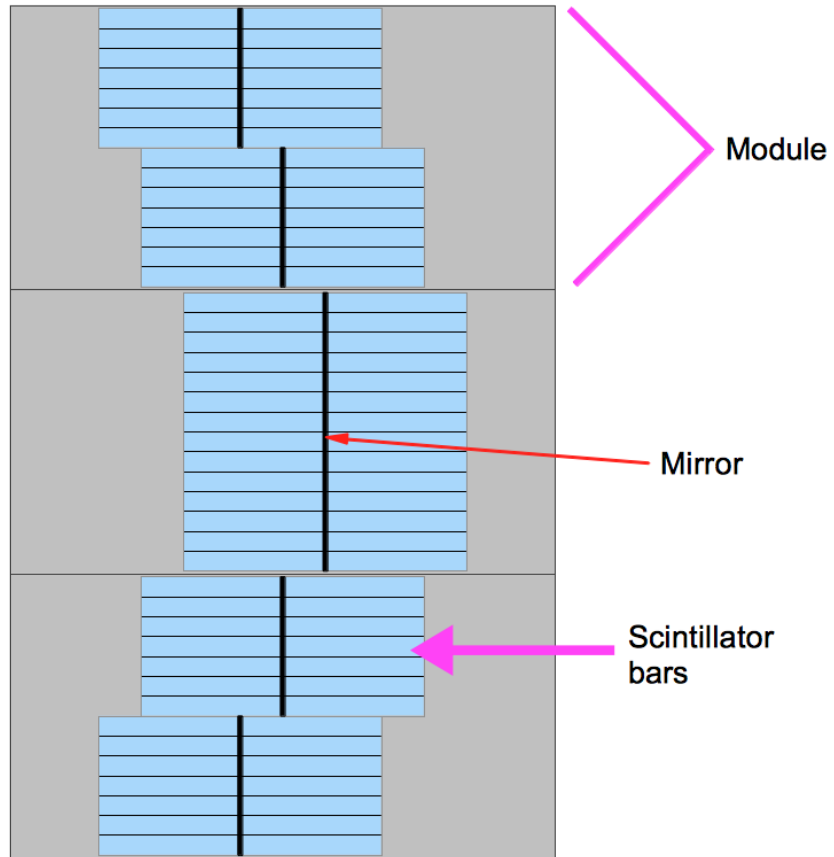


Figure 10: Diagram of scintillator bar staggering in one layer of CDet for detector acceptance matching. The general curvature of the scintillator stacks follows the right side of a circle.

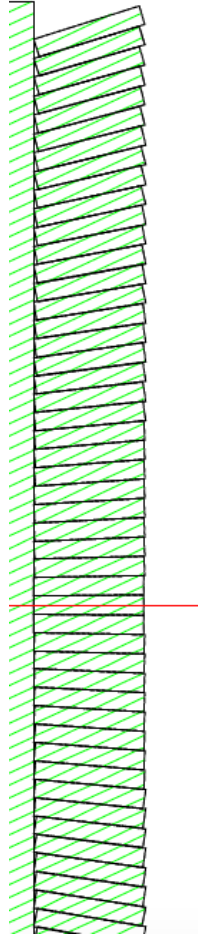


Figure 11: Diagram of paddle tilting in CDet layer. Red line is center of layer vertically. [17]

### ***Scintillator background and key design properties***

A scintillator is a substance that produces light, or scintillates, when charged particles pass through it. When a charged particle traverses scintillating material, it ionizes atoms in its path; when the electrons are reabsorbed into the ions, light is emitted. Plastic scintillator, as used in CDet, consists of plastic that is doped with “fluors,” which are compounds that fluoresce (give off light) due to ionization and reabsorption. The plastic scintillator in CDet emits in the blue-ultraviolet wavelength range. The expected scintillation yield is 500 photons per MeV [18].

A scintillator array was chosen for CDet over other tracking technologies for several reasons. The detector will be used in high luminosity experiments, so it must be fast and able to deal with high background rates [16]. The scintillator-based CDet is much faster than the alternative tracking detector technology, and it is also less sensitive to background events [16, 17]. Scintillator detection is also a reliable, well-established technology in general [16].

### ***WLS background and key design properties***

A WLS fiber is an optical fiber that absorbs light in one wavelength range and reemits it in another. The particular type of WLS fiber used in CDet is a fast blue-to-green shifting fiber called BCF-92 [19]. The fiber absorbs the blue scintillation light from the paddle, reemits it in the green range, and transports the green light to the PMT. The shift from blue to green increases the number of photoelectrons produced in the PMT, as the quantum efficiency of the PMT is larger for green than for blue photons, and thus results in a larger electronic signal from the PMT. This is an important consideration for CDet because the small size of each paddle results in a relatively small photoelectron yield.

### ***MAPMT background and key design properties***

A PMT (photomultiplier tube) amplifies a photon signal via the photoelectric effect and secondary electron multiplication. Photons enter the evacuated tube and strike the photocathode, producing photoelectrons [11]. The photoelectrons then strike the first of a series of dynodes, which multiplies them by secondary electron emission [11]. This is repeated at each dynode in the series, creating a shower of secondary electrons. A relatively high voltage difference is established between each pair of dynodes in the series to accelerate the electrons from one dynode to the next. Finally, the shower

of multiplied electrons is collected at the anode [11], and the PMT outputs the total charge signal.

A multi-anode PMT (maPMT) is a PMT containing several of the amplification systems described above [11]. It can thus multiply several signals independently. A single signal amplification channel is called a pixel. The CDet maPMTs have 16 pixels arranged in a  $4 \times 4$  matrix. These maPMTs were donated to Hall A by Fermi National Accelerator Laboratory from a decommissioned detector, so using them greatly reduced the cost of building CDet [16, 17, 20].

Since only 14 WLS fibers connect to each 16-pixel maPMT, a specific pattern was chosen for omitting two pixels and connecting the fibers to the remaining 14. All pixels on each maPMT have been tested for signal quality. Therefore, the chosen pattern omits the two worst pixels on each maPMT, whatever their location, and simply connects the fibers from the scintillator paddles to the 14 remaining pixels in numerical order. For example, pixel 4 and pixel 16 are omitted in PMT 7 on the right side of Module 1, as shown in Fig. 12 by the black numbers. The fibers from paddles 1 to 14 in the corresponding scintillator bar are then connected to the remaining pixels in ascending numerical order, as shown in the figure by the red numbers. The connection of adjacent paddles to adjacent pixels particularly necessitates the analysis of the crosstalk between pixels in order to distinguish signals shared between adjacent paddles from false signals induced in adjacent pixels.

<b>1</b> <b>1</b>	<b>2</b> <b>2</b>	<b>3</b> <b>3</b>	
<b>5</b> <b>4</b>	<b>6</b> <b>5</b>	<b>7</b> <b>6</b>	<b>8</b> <b>7</b>
<b>9</b> <b>8</b>	<b>10</b> <b>9</b>	<b>11</b> <b>10</b>	<b>12</b> <b>11</b>
<b>13</b> <b>12</b>	<b>14</b> <b>13</b>	<b>15</b> <b>14</b>	

**Pixel number (black)**  
**Paddle number (red)**

Figure 12: Example map of maPMT pixels and connected paddle fibers

### Expected detector performance parameters

The planned detection efficiency for CDet is  $\sim 99\%$  [16]. This is the percentage of signals that are detected. The detection efficiency, however, is not a set number, but a function of the threshold used during the experiment. The threshold is set with the intent to reject noise and accept real signals. In the CDet data acquisition (DAQ) system, this threshold is a charge signal threshold, which must be exceeded in order for a signal to be accepted. The appropriate threshold value must be determined using the photoelectron count distributions from the ADC calibration analysis; this is discussed in Chapter IV. However, some relevant information is already known from an older simulation of CDet performed during the design of the detector [16]. This simulation was used, among other purposes, to estimate the detection efficiency of CDet at various thresholds of energy deposition in the paddles. As seen in Fig. 13, the 99% efficiency level is met at thresholds less than about 3 MeV. To verify that

the appropriate threshold level is within this range, the ratio of photoelectron count to energy deposition obtained from the ADC calibration analysis will be used.

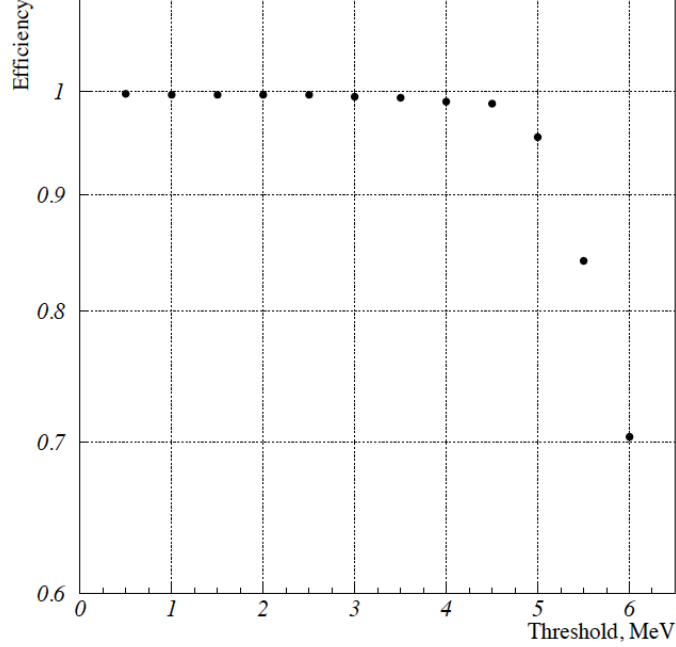


Figure 13: Estimate of detection efficiency as a function of energy threshold [16]

The mirror placed at the inner ends of the scintillator bars, designed to increase reflectivity inside each bar, was specifically intended to increase the overall efficiency of the detector and to maintain that efficiency across the whole length of the bar, regardless of where along the bar a primary particle passed through. Between the mirror and the reflective material wrapping each bar and paddle, CDet is expected to have high “optical efficiency” such that a particle depositing a given amount of energy in any part of the bar will produce the same signal.

Regarding the maPMTs, the level of crosstalk is expected to be low. According to the specifications reported in the manufacturer’s handbook [11], the amount of crosstalk

in adjacent pixels is less than 3% of the actual signal when the maPMTs are used with the same high-voltage setting as in the CDet test data.

### Test setup at JLab

Each module of CDet is tested separately, one half at a time. The module is laid flat, with the front side facing up, and tested with cosmic rays. One half, consisting of 196 channels, is connected to a data acquisition (DAQ) system.

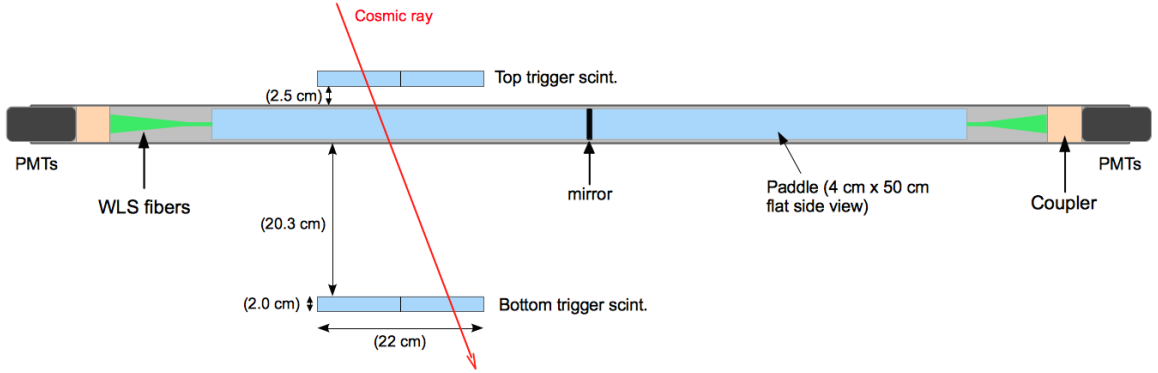


Figure 14: Side view cross section diagram of module test setup

The trigger system for the test setup consists of two pairs of wide scintillator paddles. One pair is placed above the module, and the other pair is placed below. Each trigger paddle is 11 cm wide and 2 cm thick. The trigger paddles in each pair are placed next to each other, giving a total trigger width of 22 cm on top and bottom. Both the top and bottom trigger scintillators are placed across the centers of the bars in the half-module being tested. The lower surface of the top trigger scintillator is 2.5 cm above the upper surface of the module, and the upper surface of the bottom trigger scintillator is 8 inches below the lower surface of the module. In order for the DAQ system to be triggered, a signal must be present in both the top and bottom trigger



scintillators. When a trigger occurs, the DAQ system reads out all 196 channels of the half-module.

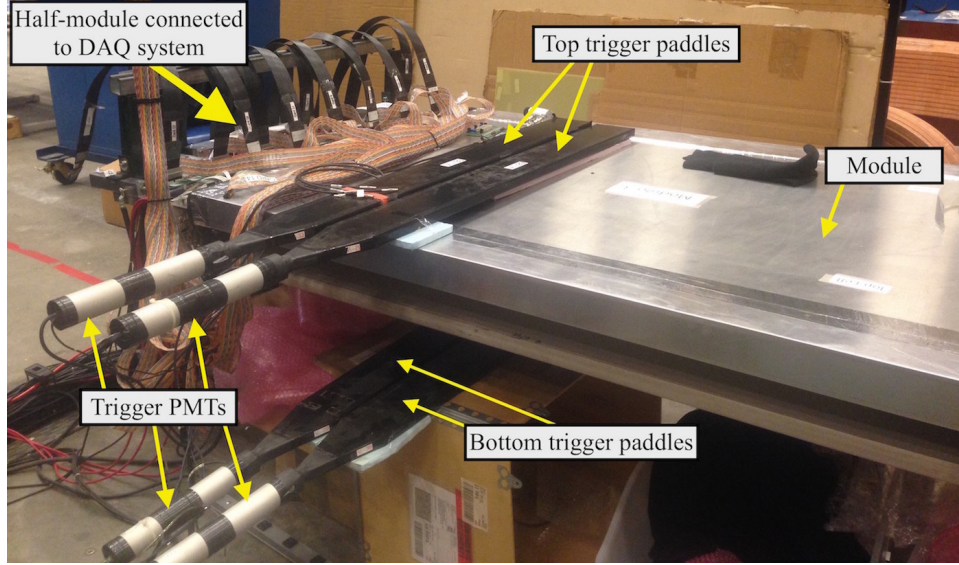


Figure 15: Photograph of module test setup at JLab

### Description of test data

The electronic signals from each maPMT go into a circuit board called a NINO card, which further amplifies each signal. If a trigger also occurs, the amplified signals are then sent to the ADCs for conversion. Each signal is integrated over a set time interval to obtain the total charge, and the ADC then converts the integrated charge into the corresponding ADC channel, which is an integer value between 0 and 4096. The conversion factor in the ADCs is specified to be 50 pC per ADC channel.

The ADC channels are the main raw data of interest. However, there is another DAQ device that produces raw data: a time-to-digital converter or TDC. Each NINO card also has a discriminator unit that produces a logic signal if the electronic signal passes the specified threshold. If the threshold is met, the logic signal is sent to the TDC to indicate a “start time.” Additionally, when the data readout begins, the trigger

electronics generate their own logic signal. The trigger logic pulse is too long to be useful, so another discriminator converts it into a much shorter pulse. Two “copies” of the short logic pulse are then sent out. One copy goes to the TDC, after a certain amount of delay, to indicate a “stop time.” The difference between the stop time and start time is converted into a corresponding integer called a TDC channel. As with the ADC channels, the TDC channel range is from 0 to 4096. The various delays have been configured such that the difference between the stop and start times results in a TDC channel of around 900; if, however, the original PMT signal does not meet threshold and no start signal is sent out, the corresponding TDC channel is 0.

The other copy of the shortened trigger logic pulse is sent to another discriminator which lengthens it to the time interval set for the ADC integration. Then it is sent, through an appropriate delay, to the ADCs. When this logic pulse arrives at the ADCs, it “opens the gate,” and the charge integration begins. Integration continues until the logic signal stops, at which point the gate is “closed” and the integration also stops.

Because all data channels in the half-module are read out every time the DAQ system is triggered, most of the recorded ADC data is actually noise from all the readouts of pixels with no hits. Some of this noise can be removed by using the corresponding TDC spectra to separate out all the ADC data resulting from PMT signals that did not pass threshold in the NINO cards. However, the threshold used for the test data is relatively low, and a significant amount of noise still remains. When the ADC data is plotted for each pixel, this noise appears as a large, narrow peak at the low end of the spectrum. This peak is called a pedestal. The pedestal width on each pixel is necessary information for determining the proper thresholds that should ultimately be used in the DAQ electronics to eliminate noise in the real experimental setup of CDet.

## CHAPTER III: GEANT4 SIMULATION

### Design of CDet simulation

The Geant4 simulation of CDet consists of the radiation transportation module only. The primary particles are generated by a different software tool and then read in by the Geant4 detector simulation, and the simulation outputs pure physics data without converting it into electronic signals. The Geant4 code consists of a main program and various classes that construct the detector, specify the detector materials and their properties, read the primary particles from the primary input file, specify what physics processes to include, process hits in the detector, record event data, and output that data to a file. The code also produces a 3-D visualization of the simulated detector model with particle tracks.

#### *Detector model design overview*

The simulation models one bar of the coordinate detector. This subset of the detector was chosen for the simulation because one bar is the basic unit of CDet and because the test data is analyzed one bar/maPMT at a time. Therefore, the simulation results are comparable to the test data results. The components of the simulated bar include 14 scintillator paddles, their WLS fibers, the mylar wrapping, and the end mirror. Instead of modeling a multi-anode PMT, 14 tiny, individual PMTs are coupled to the WLS fibers to ensure that each simulated pixel is completely independent of the others. No extra light wrapping is necessary around the WLS fibers, as the wavelength-shifting core is surrounded by a cladding that produces total internal reflection. To match the test data, the simulation is designed to model the passage of cosmic rays through the detector. Therefore, the bar is oriented sideways (paddle edges up) just like it would be in the full module in the real test setup. To complete

the simulated test setup, a single piece of scintillator is placed above the center of the bar as a trigger paddle. While this does not match the trigger system used in the CDet test setup, the simulation code was actually originally written for a similar, but different, scintillator detector and subsequently modified to simulate a CDet bar. Because much of the existing code was designed for the presence of only one trigger paddle, the mismatched trigger system was left alone for ease of coding. Compensation for the mismatched geometry is instead included in the analysis code.

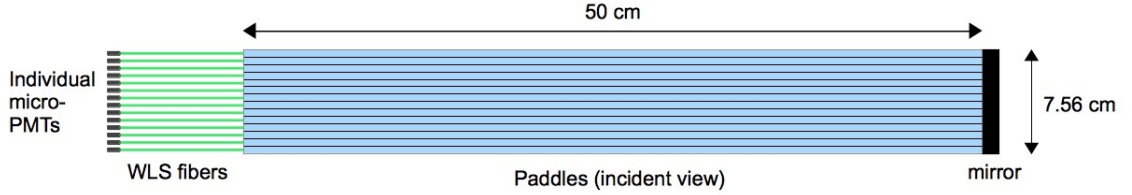


Figure 16: Top view diagram of simulated CDet bar

### Detector construction

In Geant4, all physical components of the detector model are created using two basic kinds of objects: volumes and optical surfaces. Volumes describe the three-dimensional detector components, and surfaces describe optical interfaces or boundaries between components. A volume is created with specified dimensions and then filled with a material. An optical surface is created with general interface properties, and specific surface properties are assigned to it. By themselves, volumes and surfaces are sets of physical attributes. An optical surface can be assigned to the actual physical surface of any volume intended to have those surface properties. A volume becomes part of the detector model when it is placed in a particular location in a coordinate system; a volume can be placed as many times as necessary to create identical detector components (e.g. the scintillator paddles in the CDet bar). Each

placed copy of a volume is assigned a unique ID number that is used to identify that particular component when the simulation runs. In addition to the detector volumes, a “world volume” is always created to house the entire detector model [21] and is usually filled with air. All the detector components are placed inside this volume according to its internal coordinate system with the origin at its center.

The world volume housing the simulated CDet bar is a cubic room 3.0 meters on a side, which is filled with air. A right-handed Cartesian coordinate system is used, with a slightly unconventional orientation such that the  $y$ -axis is vertical and the  $x$  and  $z$  axes are horizontal. The scintillator bar paddles are each 50.0 cm long, 4.0 cm wide, and 0.5 cm thick, with a hole down the center measuring 0.19 cm in diameter. The trigger paddle is 10.0 cm wide, 1.0 cm thick, and 27.56 cm long. The scintillator volumes are filled with a user-defined material modeled on a detailed description of a common scintillator plastic known as BC-408 [18], which is very similar to the scintillator plastic used in CDet. The aluminized mylar wrapping for the paddles is 0.02 cm thick and is broken into a set of rectangular layers. Straight aluminum is used for the material, as the important properties of the wrapping are specified in the optical surface used for the mylar. The WLS fibers are specified in two parts: the wavelength-shifting core and the outer cladding that produces total internal reflection. The core is 0.16 cm in diameter, and the outer cladding is 0.18 cm in diameter. Each fiber is 60.0 cm long. The core material is acrylic, and the cladding material is polyethylene. The last component of the bar, the mirror, is 0.2 cm thick, 4.0 cm tall, and 7.56 cm wide, so it exactly covers the end of the bar. The mirror material is aluminum, with an optical surface assigned to specify the reflectivity.

The 14 scintillator bar paddles are placed side by side, parallel to the  $x$ -axis, with a layer of mylar on either side of each paddle. Two single layers of mylar are also placed on the top and bottom sides of the full bar, covering the edges of the paddles.

Thus, there are two layers of mylar between each pair of paddles, and one layer of mylar covering the top, bottom, and long sides of the whole bar. The trigger paddle is centered across the bar, its length parallel to the  $z$ -axis, with 1.0 cm of space between the bottom of the trigger and the top of the bar. Mylar sheets cover the top, bottom, and long sides of the trigger paddle. The mirror is placed up against the back end of the bar. The 14 fibers are placed inside the holes through the paddles in the bar, with the back ends up against the mirror and the front ends emerging from the paddles. The fiber core is simply nested inside the cladding.

The PMTs in the simulation do not actually model photomultipliers. They are pieces of glass which model the front-end initial photon absorption in real PMTs. The relevant properties are specified by the optical surface attached to the PMT volumes. The PMT components for the WLS fibers are 0.3 cm thick and 0.19 cm in diameter, exactly matching the size of the fibers. The PMT for the trigger paddle is also 0.3 cm thick and has the same area dimensions as the end of the trigger paddle (10.0 cm wide  $\times$  1.0 cm thick). The WLS fiber PMTs are placed up against the ends of the WLS fibers, and the trigger paddle PMT is placed up against one end of the trigger.

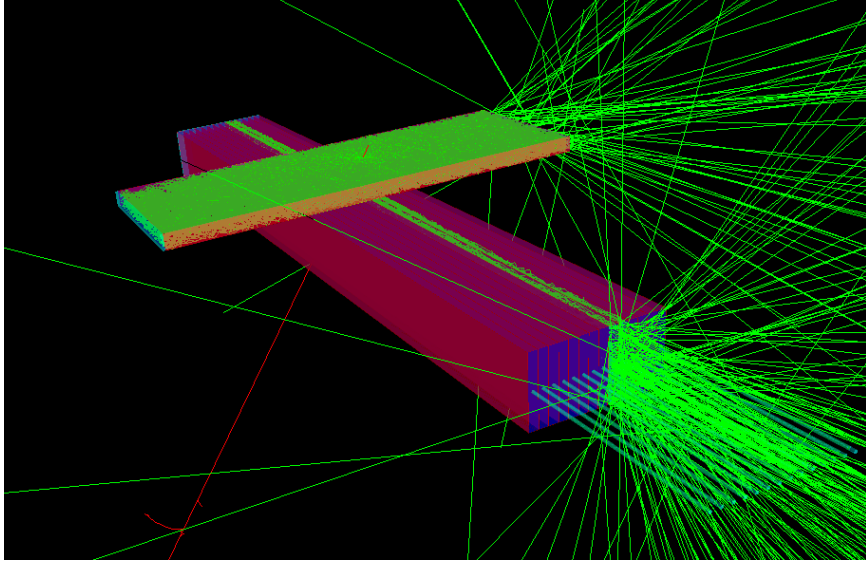


Figure 17: 3-D visualization of Geant4 CDet bar model. Red line poking through center of setup represents a single primary muon track. The green lines represent photon tracks emerging from the uncovered ends of the scintillator paddles.

### *Material properties*

In Geant4, default materials can be used, or else materials and their properties are specified by the user. A user-defined material is created by specifying its elemental or atomic composition and its density. Properties are then assigned to the material; some common properties include index of refraction, absorption length, and reflectivity. These properties are described over a range of energies, so they are specified as arrays of values that correspond to different particle energies. In the case of optical properties, the particles are photons.

Optical boundaries between materials are described by optical surfaces [22]. Surfaces are always defined by the user. When a surface is created, the type of interface must be specified; this indicates the categories of the materials on either side of the boundary, whether it is two dielectrics, a dielectric and a metal, etc. [22, 23, 24]. The “finish” on the surface can also be specified [22]. The finish describes the smoothness or roughness of the surface, as well as the presence of certain paints, glues, or films [22].

After a surface is created, more specific properties are assigned to it. Examples of surface properties include reflectivity and efficiency.

In the CDet simulation, the scintillator plastic, WLS fiber materials, and PMT glass are user-defined; Geant4's default description of aluminum is used for the mylar wrapping and the mirror. The range of photon energies used in describing the optical properties of the user-defined materials is specified in two different ways. For the WLS fiber materials, the energy range is specified as an array of 50 energies from 2.00 eV to 3.47 eV; for the scintillator plastic and PMT glass, the energy range is specified as an array of 12 energies from 3.44 eV down to 2.08 eV. The scintillator plastic is modeled on the specifications of BC-408 scintillator material [18]. Its density is 1.03 g/cm<sup>3</sup>. It has a constant index of refraction of 1.58 and a constant absorption length of 210.0 cm over all given energies. The scintillation yield, which is the number of photons emitted per unit of energy deposited, is 500 photons/MeV [18]. The time delay between a charged particle interaction and the emission of scintillation light is 1.0 ns. A distribution is also specified which indicates the probability of emitting scintillation light at each of the 12 given photon energies; this distribution peaks at 2.92 eV, which corresponds to a wavelength around 420 nm. As seen in Fig. 18, most of the scintillation light is in the blue range.

The polyethylene cladding on the WLS fibers has a density of 1.20 g/cm<sup>3</sup>, a constant refractive index of 1.49, and a constant absorption length of 20.0 m over all given energies. The wavelength-shifting acrylic core of the WLS fiber has a density of 1.19 g/cm<sup>3</sup> and a constant refractive index of 1.60 over all given energies. It has a widely-varying absorption length which decreases from 1.40 m to 0.2 mm over photon energies of 2.00 eV – 2.96 eV and then increases up to 2.8 mm as photon energies increase to 3.47 eV. The time delay between photon absorption and reemission is 0.5 ns. A distribution is specified with the probabilities of reemitting photons at all 50



given photon energies. The emission distribution, converted to wavelengths, is shown in Fig. 19. Both of the emission distributions for the scintillator and the WLS fibers were obtained by reading points off plots provided by the respective manufacturers of the real CDet materials.

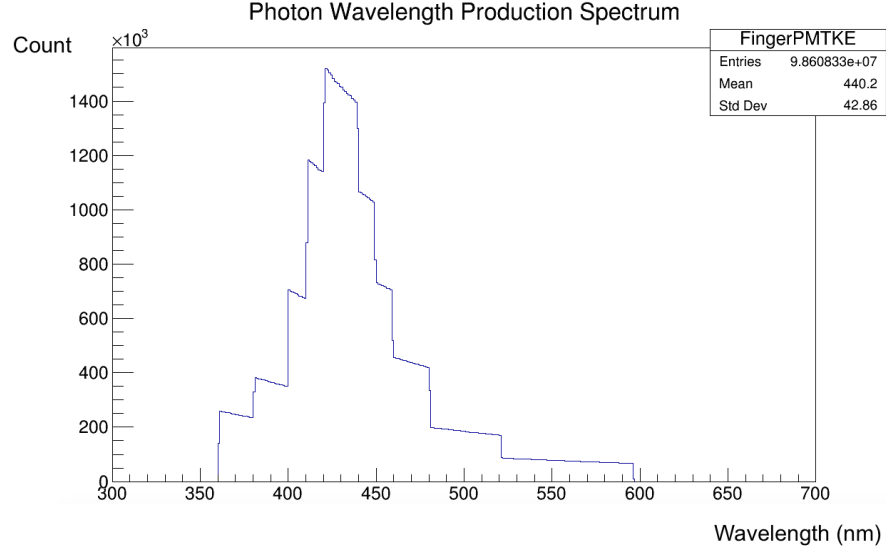


Figure 18: Distribution of scintillation wavelengths (in nanometers)

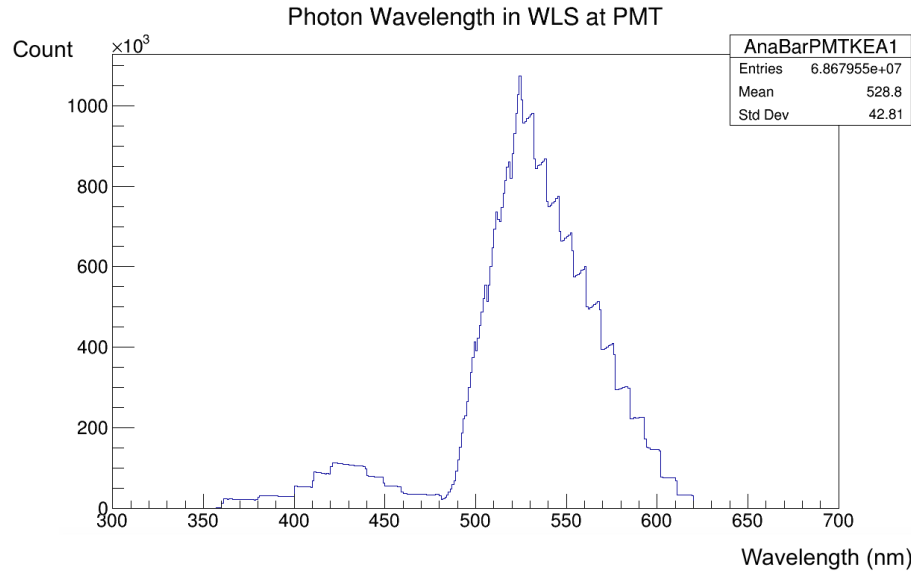


Figure 19: Distribution of WLS fiber reemission wavelengths (in nm)

The PMT glass has a density of  $2.55 \text{ g/cm}^3$ . Its absorption length of 420.0 cm is constant over all 12 energies. The index of refraction varies over four values from 1.525 to 1.534 with decreasing photon energy. The glass reflectivity varies over five values from 0.0846 to 0.0909 with decreasing photon energy. The PMT optical surface is given a “polished” finish to model it as perfectly smooth [22]. The interface type is modeled as a transition between a dielectric (the scintillator or WLS plastic) and a metal, as this allows the glass window to also model the surface of the photocathode in a real PMT at the same time. The quantum efficiency (photon detection probability) of the real PMTs when connected to the WLS fibers is 13.0%, so the “quantum efficiency” (transmission probability) of the simulated PMT surface is 0.13. The surface is also assigned a reflectivity of 0.0.

The aluminized mylar sheets are modeled as aluminum sheets because only the surface properties are important. The mylar surface is specified as an interface between a dielectric (the scintillator plastic) and a metal (the aluminum sheet). The reflectivity is 0.9 (90%), and the transmissivity is 0.0. Both of these parameters are constant over all given energies.

The mirror is also modeled as an aluminum plate, with all relevant properties contained in the optical surface. The mirror surface is specified as a dielectric-metal interface. The reflectivity is 1.0 (100%), and the transmissivity is 0.0; both are constant over all given energies.

### **Primary generation**

The primaries in this simulation are meant to model cosmic rays; for simplicity, all generated primaries are muons. They are given initial coordinates 1.0 cm above the top surface of the trigger paddle and within a  $9.0 \text{ cm} \times 12.0 \text{ cm}$  horizontal region where the trigger paddle overlaps the scintillator bar. The magnitudes and directions

of their initial momenta follow empirical fits to experimental data on real cosmic rays. The primaries are generated using a software package called ROOT. User input to the primary generation code specifies the number of primaries to be generated.

## ***ROOT***

ROOT [25] is a data processing framework created at CERN. It has a broad range of capabilities for data analysis, simulation, and data storage. ROOT has its own special type of file for storing data. ROOT files use a tree structure that allows large quantities of data to be accessed quickly [26]. The generated primaries, the output data from the simulation, and (after a certain amount of processing) the CDet test data are all stored in ROOT files. For data analysis, ROOT's extensive library can be used to easily perform calculations, generate random numbers, create graphs and histograms, and fit plots with functions. ROOT, like Geant4, is based on the C++ language, allowing the two frameworks to accomplish different aspects of the same simulation quite seamlessly.

## ***Generation of cosmic muons***

The initial position and momentum of each primary muon are chosen randomly from specified distributions. The initial  $y$  position is 1.0 cm above the top surface of the trigger paddle. The initial horizontal  $x$  and  $z$  coordinates follow uniform distributions. The  $x$  distribution spans 9.0 cm centered across the width of the trigger paddle, covering approximately one-fifth the length of the scintillator bar. The  $z$  distribution spans 12.0 cm along the length of the trigger paddle, covering more than the width of the scintillator bar. The initial  $x$  and  $z$  coordinates are chosen randomly within these ranges.

The momentum magnitude distribution follows an approximated piece-wise empirical fit to experimental data [27]. As shown in Fig. 20, it consists of a uniform distribution

for momenta between 0.5 GeV/c and 3.5 GeV/c, and a decaying power function for momenta between 3.5 GeV/c and 20.0 GeV/c. The power function distribution  $P(p)$  is given by

$$P(p) = p^{-2.7}, \quad (1)$$

where  $p$  is the momentum magnitude. This distribution is specified in the primary generation code as two separate functions, each valid within their respective intervals. To determine what proportion of the whole distribution is uniform, the integral of the uniform part is divided by the sum of the integrals of both parts to obtain a uniform-to-total ratio. This is necessary for generating a momentum value from the distribution. When choosing the momentum of a muon, two iterations of random numbers are used. First, a random number is generated between 0 and 1.0. If this number is less than the uniform-to-total ratio, a momentum value is randomly chosen from the uniform distribution; otherwise, a momentum value is randomly chosen from the power distribution.

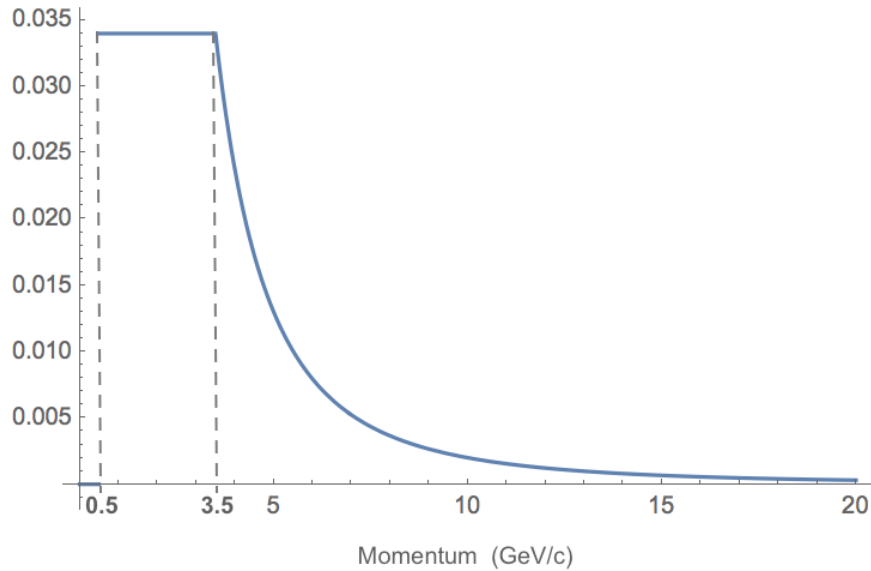


Figure 20: Momentum distribution for cosmic muons

Regarding the momentum direction, the polar angle  $\theta$  and azimuthal angle  $\phi$  have single-function empirical fits. The fit to the  $\theta$  distribution used for the primary generation is a cosine-squared function [27]. In the CDet model,  $\theta$  is measured with respect to the positive  $y$ -axis, maintaining its convention as the angular deviation from the vertical. The angle  $\theta = \pi$  is straight down, and  $\theta = \pi/2$  is horizontal, so the  $\theta$  distribution is given the limits of  $\pi/2 \leq \theta \leq \pi$ . The distribution for  $\phi$  is simply a uniform distribution with limits  $0 \leq \phi < 2\pi$ . The angle  $\phi$  is measured in the horizontal  $xz$ -plane with respect to the positive  $x$ -axis. The values of  $\theta$  and  $\phi$  for a generated muon are chosen randomly from the respective  $\cos^2\theta$  and uniform distributions, within their respective limits.

The primary muon momenta are generated in spherical coordinates because the empirical distributions are measured and reported in spherical coordinates. However, after a set of momentum coordinates are generated for a given primary, they are converted from spherical to Cartesian coordinates. The energy of the primary is also calculated from the momentum magnitude and the muon mass. Finally, the initial position and initial momentum coordinates (both Cartesian), the initial energy, and the muon particle ID number are saved and written to the primary generation output file, which becomes input to the Geant4 simulation.

The Geant4 simulation reads in the primaries from the specified input file. It reads the particle ID number, initial position coordinates, initial momentum coordinates, and initial energy of each primary and creates a Geant4 “primary vertex” for each one. This vertex is generated using something called a “particle gun,” as the primary is “shot” into the detector with its specified momentum and energy.

## Physics processes

All the physics processes in the simulation come from Geant4’s extensive library. The most important processes in the CDet simulation are optical processes. Photons are generated in the detector, and then they interact with the detector materials. Photons, specifically termed “optical photons” in Geant4 [23], are primarily generated by the scintillation process in the paddles. The Geant4 scintillation process uses the parameters, such as scintillation yield, which are specified for the scintillator material. The scintillation process also includes a correction using Birks’ law. Birks’ law is an empirical relation of photon yield per unit path length as a function of energy deposited per unit path length by a particle in a scintillator; most importantly, it is non-linear in regions of high energy loss [28].

Cerenkov radiation is also included as a secondary photon production process, as most primaries will generate Cerenkov radiation as they pass through the scintillator material. However, far fewer Cerenkov photons will be produced than scintillation photons, and the narrow cone of Cerenkov light is unlikely to interact significantly with the WLS fibers, so Cerenkov radiation is not a concern regarding noise in the detector. It is simply included in the simulation for completeness.

Once optical photons are generated in the scintillator, they undergo various interactions. Five Geant4 processes or process groups are specified in the simulation for photon interactions: absorption, boundary interactions, wavelength shifting, Rayleigh scattering, and Mie scattering. Absorption, boundary interactions, and wavelength shifting are the main processes that take place in the detector. The Geant4 absorption process uses the specified absorption length for each material in the detector. When a photon is absorbed, it is simply “killed” within the simulation after traveling some selected distance [22, 23]. Geant4 has three processes that can occur at boundaries between media: absorption, reflection, and refraction. The ones that are applicable

at a given boundary depend on the materials forming the boundary. If a photon is crossing from a dielectric to a metal (e.g. scintillator→mirror, WLS fiber→PMT), it can either be absorbed or reflected [22, 24]. If, however, a photon crosses from one dielectric to another (e.g. scintillator→WLS fiber), it can either be reflected or refracted [22, 24]. The Geant4 wavelength shifting process uses the parameters specified for the WLS fiber material to absorb photons that came from the scintillator and reemit new photons in the new wavelength range [23].

Rayleigh scattering and Mie scattering are secondary processes included, like Cerenkov radiation, for completeness. While not expected to affect the detector results much, if at all, they might affect the tracks of photons within the detector, which is important for the particle transport process internal to the simulation. The Geant4 process for Rayleigh scattering (elastic scattering off atoms/molecules) keeps track of the polarization of the photon before and after scattering [23, 24]. Mie scattering (scattering off spherical particles) in its exact form is too ungainly for Monte Carlo simulations, so an approximation is used in the Geant4 implementation [24].

## Detection

In Geant4, particle detection is accomplished using “sensitive detectors.” A sensitive detector is any detector component that responds to hits, where “hits” are interactions from which data is recorded. Because all internal processes are known in a simulation, any detector component can become a sensitive detector, including components that do not provide a response in the real experiment. In the CDet simulation, the PMTs and the scintillator paddles (including the trigger paddle) are the sensitive detectors. This allows the simulation to output data on the internal processes within the scintillators (e.g. energy deposited by primaries) as well as the usual photon detection at the PMTs.

In terms of the code, a sensitive detector (SD) is an object that processes hits for a particular type of detector component. To achieve the actual sensitive detector functionality, each SD object is registered in the simulation as a sensitive detector and is assigned to the appropriate detector component(s).

### ***Hits and hit processing***

A “hit,” most generally, is an interaction of a particle with any sensitive detector component. This could be a physics interaction within the detector medium, or it could be a boundary interaction as the particle enters or exits the medium. There are two kinds of hits in the CDet simulation corresponding to the two sensitive detector types: scintillator hits and PMT hits. While a hit, strictly speaking, is a physics interaction, the simulation stores a hit as an object containing a set of data describing the interaction. All resulting scintillator and PMT hits from each primary event are stored together in respective lists called “hit collections.”

Different particles generate hits in the scintillators and the PMTs. The PMT SD detects only optical photons, while the scintillator SD detects all other particles that are not optical photons. When the primaries pass through the scintillator material, they produce secondary particles that may also interact with the scintillator. Most of the secondaries are electrons ionized off atoms in the scintillator. The scintillator SD detects the secondaries as well as the primaries.

A charged particle can interact with the scintillator material along its entire path through the paddle. One scintillator hit, therefore, corresponds to the interaction of the particle during one “step” of transportation through the paddle. As a result, a single primary event can produce many hits in a single paddle due to the generation of secondaries and the number of steps each particle takes through the paddle. For each hit, the following data is recorded: the identification of the particle, the energy



deposited, the momentum vector of the particle, the position coordinates of the particle at both the beginning and end of the step, the time when the step occurred, and the ID number of the scintillator paddle in the CDet bar model. Each time a hit occurs, a new hit object is created and the hit data is logged; then the hit is added to the hit collection for that event.

For the PMT sensitive detector, hits are less complicated. The PMT SD only detects photons, and each photon only interacts once with the PMT surface. Furthermore, not all photon interactions with the PMT surface count as detections. If a photon is absorbed by the PMT, it is detected and assumed to produce a photoelectron; if the photon is simply reflected off the PMT, however, the interaction is ignored and nothing happens. Therefore, the PMT only detects the photons that are absorbed, and the proportion of photons which are absorbed, out of all photons striking the PMT, is determined by the quantum efficiency specified for the PMT surface, which is 0.13. This means that only 13% of all photons interacting with the PMT surface are actually detected. For the PMT SD, then, a hit is defined as all photons detected by one PMT during one event, rather than as the detection of an individual photon. Therefore, the number of PMT hits in an event equals the number of PMTs that detected photons. The data for one PMT hit consists of the number of photons detected, the kinetic energy of each photon, and the PMT ID number in the CDet bar model. Again, it is assumed that one photon detected corresponds to one photoelectron emitted.

Because one PMT hit includes multiple photons, hit processing is slightly more involved for PMT hits than scintillator hits. Each time a photon is detected, the PMT SD checks whether that particular PMT already has a hit or not. If it does not, a new PMT hit is created, the data is logged, and the hit is added to the PMT hit collection. The ID number of the PMT and the location of the hit in the collection

are also logged for future reference; as that PMT detects more photons, their data will be added to the hit for that PMT. If, however, that PMT already has a hit, the number of photons is simply incremented for that hit, and the kinetic energy of the new photon is logged.

### Resulting simulation data

At the end of each primary event, all hit data is read out into lists corresponding to each type of data. For the PMT hits, the number of photons detected by each PMT is read into a list, and the kinetic energy of each photon is read into a two-dimensional list; both lists are structured such that the PMT ID numbers are specified by the list index. For the scintillator hits, all the data categories are read into their respective lists, a few of which then undergo minor processing. A single set of position coordinates  $(x, y, z)$  is computed for each hit by taking the averages of the position coordinates of the step endpoints. The number of hits is also counted as each hit is processed to give the total number of scintillator hits in that event. After all processing and list-filling is finished, the data of interest is written out to a ROOT file, including data on the primary muon. The recorded data on the primary muon are its initial energy, angular coordinates  $\theta$  and  $\phi$  of its momentum, and its particle ID number (for verification). The recorded data on the PMT hits are the number of photons detected by each PMT (which equals number of photoelectrons emitted), the energy of each photon, and the ID number of the last PMT in the PMT hit collection. The recorded data on the scintillator hits are the total number of hits in all paddles and, for each hit, the particle ID number, the ID number of the paddle, the energy deposition in the paddle, the position coordinates of the hit, and the time of the hit. A summary of the data recorded for each event is given in Tab. 1.

Table 1: Summary, by category, of simulation data recorded from each primary event

<b>Primary muon</b>	
Initial energy	
Angle $\theta$ of momentum	
Angle $\phi$ of momentum	
Particle ID number	
<b>Detector Hits</b>	
Total scintillator hit count	
ID number of last PMT hit	
<b>Per PMT hit</b>	<b>Per scintillator hit</b>
Num. photons/photoelectrons	Particle ID
Energy of each photon	Paddle ID number
	Energy deposition
	Position $(x, y, z)$
	Time

## CHAPTER IV: ANALYSIS

### Analysis background

All the analysis code is written using the ROOT framework. Prior to the start of this thesis, two analysis codes already existed: one to analyze data from the simulation, and one to analyze the CDet test data. Most of the analysis performed by these codes consists of placing cuts on the data, plotting and fitting histograms, and extracting parameters from those fits. The analysis performed in this project builds on these two codes.

#### *Test data analysis code and vertical track selection*

The test data analysis code produces plots of the ADC and TDC distributions. Some of these plots are raw distributions, while others have cuts applied and fit functions added to them. The data is analyzed from only one maPMT at a time, so the analysis shows the results from a single scintillator bar.

For the purposes of this thesis, the most important data is the ADC data. There are two main cuts placed on it during analysis. The first of these is the so-called “TDC cut,” which uses the TDC channel corresponding to each ADC channel to determine whether to keep that ADC signal in the analysis or to ignore it as noise. If the original CDet PMT signal passed the set threshold, the resulting TDC channel is around 900, and the corresponding ADC signal may represent a real event. However, if the original PMT signal did not pass the set threshold, then the resulting TDC channel is simply zero, and the corresponding ADC signal is known to represent noise. In the analysis, therefore, a cut is placed such that ADC channels with corresponding TDC channels in a suitable interval are kept, while ADC channels with corresponding TDC channels outside that interval are ignored. This suitable interval is determined by looking at

plots of the raw TDC data distributions. A “minimum” and “width” are chosen based on the position and width of the distributions (in units of TDC channels), and these two numbers specify the start of the interval and the size of the interval, respectively.

The other cut placed on the ADC data implements a restriction deduced from geometry. The raw ADC spectra represent primary particles that have passed through the paddles at a wide range of angles. However, the events of interest are from primaries that pass through one paddle only. In the cosmic ray test setup, this is equivalent to primary events with vertical or near-vertical tracks. Hence the ADC spectra of interest include, in principle, only near-vertical primary events, and a cut must be applied to the data to remove other events. Primaries with near-vertical tracks deposit the most energy into a paddle since they travel through its full thickness (4.0 cm), so they will produce the largest ADC signals. Since almost all the energy deposited will be in a single paddle, little to no signal will result from the neighboring paddles. Primaries with tracks at shallower angles, however, pass through narrower paddle cross-sections, depositing smaller amounts of energy and resulting in ADC channels that are somewhere between the pedestal and the region of near-vertical tracks. Because such primaries also travel through multiple paddles, depositing some energy in each, signals of significant size will result from the paddles adjacent to the paddle being analyzed. Therefore, near-vertical tracks can be selected for each paddle by placing a threshold on the allowed ADC signal size, per event, coming from the two neighboring paddles. If the signals in both neighbors are less than the threshold, the event is kept, but if the signal in either neighbor exceeds the threshold, the event is ignored. Because this threshold filters the data from each paddle based on the signal in the neighboring paddles, it is called the “neighbor cut.” In the code, for each event in the bar being analyzed, the analysis routine loops through all the paddles in the bar and applies the neighbor cut to each. If a paddle passes the neighbor cut, its ADC channel value is added to a histogram for vertical track signals in that paddle.

When all the ADC data has been processed and plotted for the 14 paddles, each resulting ADC spectrum has two visible peaks, which can be seen in Fig. 21. The shorter peak on the right is the vertical track ADC distribution, and the tall, narrow peak on the left is the pedestal. The spectrum is normalized such that the pedestal is centered approximately at zero. The signal is separated from the noise, allowing the experimental threshold to be appropriately determined.

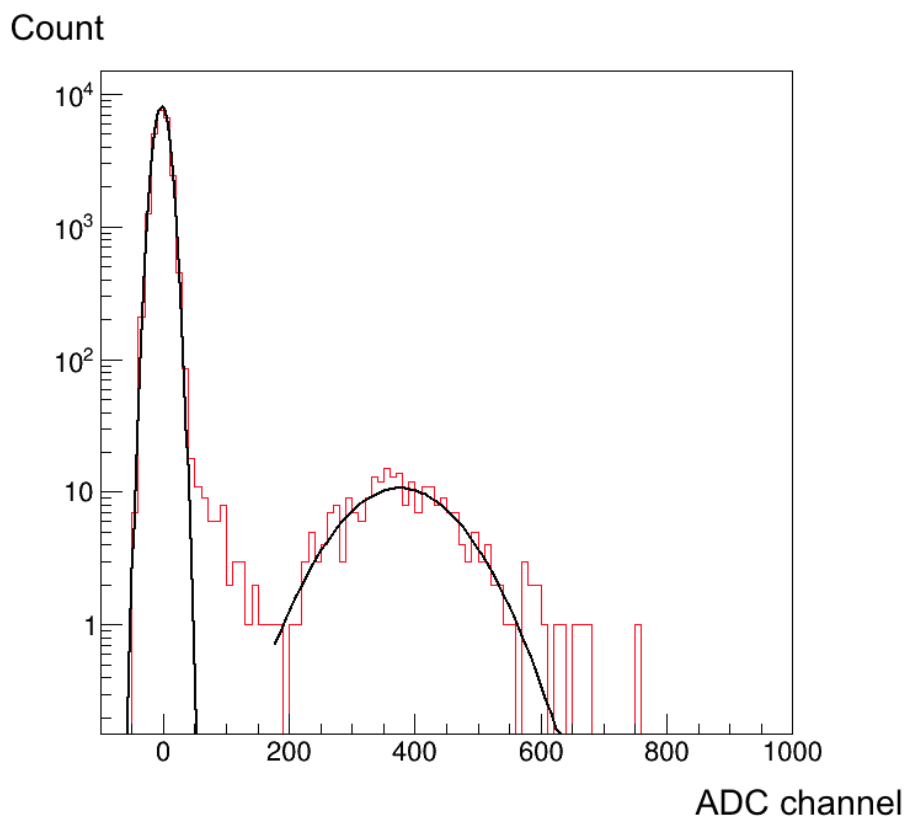


Figure 21: Example of vertical track ADC distribution for one paddle. The  $x$ -axis shows the ADC channel spectrum, and the  $y$ -axis shows histogram counts. Black curves are Gaussian fits.

After the cuts have been placed on the ADC data and the vertical track ADC spectra have been created for each paddle, fit functions are applied to the two peaks in each spectrum (black curves in Fig. 21). Both the vertical track distributions and the

pedestals are roughly Gaussian in shape, so they are fitted with Gaussian functions. The fit parameters are extracted from the fits to the pedestals and are used to make suitable choices for the ranges of the fits to the vertical track peaks, thus making the vertical track peak fitting procedure more robust. The fit parameters are then extracted from the fit to each vertical track distribution. The means of the vertical track distributions are particularly important for the calibration analysis, as the mean ADC channel in each vertical track distribution corresponds to the mean energy deposited by near-vertical track primaries.

### ***Simulation data analysis code***

The simulation analysis code produces an assortment of plots to analyze and verify the behavior of the simulation. The most important of these include photoelectron (PE) count distributions, energy deposition distributions, and a plot of energy deposition vs. PE count. Other useful plots include distributions of light wavelengths in the scintillator paddle and in the WLS fiber (see Figs. 18 and 19 in Chapter III), as well as a distribution of paddle multiplicity (where “multiplicity” is the number of paddles with a hit due to a single primary). Other verification plots include hit position distributions, hit count distributions, plots of energy deposition or PE count in the trigger scintillator vs. a detector paddle, and a distribution of particle ID number. Plots verifying the behavior of the primaries include distributions of their initial position and momentum coordinates, a distribution of the primary initial energies, and a distribution of the primary particle ID numbers (which should all be the same).

Because the trigger condition is not implemented in the CDet simulation, it is implemented in the analysis code. As each primary event is read, the code checks if a hit is present in both the trigger paddle and any of the paddles in the bar. If this condition is met, the event is considered to have produced a trigger, and the event is analyzed. If the condition is not met, then the event is ignored. (The compensation

mentioned in Chapter III for the mismatched trigger geometry between the CDet test setup and the simulation model was not implemented in the original simulation analysis.) An exception to the trigger condition is made for the analysis plots of the primary initial conditions; all primaries are included regardless of whether the event produced a trigger or not.

One of the most important sets of plots are the PE count histograms. They show the distribution of the number of photoelectrons per event for all events in one paddle/PMT that produced a trigger. There are 14 histograms, one for each paddle/PMT. Each PE count data point is statistically smeared according to a Gaussian function that models the pedestals in the CDet ADC distributions. The standard deviation of the smearing function was chosen to approximate the same proportion of the whole distribution as the ADC pedestals. When the raw PE count distributions are plotted, the top of the “pedestal” is visible at the low end of the spectrum (Fig. 22); however, the rest of the distribution slopes down with increasing PE number until it drops off on the upper side of the place where the “vertical track peak” should be. The raw distribution does not match the shape of the ADC vertical track spectrum, as expected, because no cuts are applied.



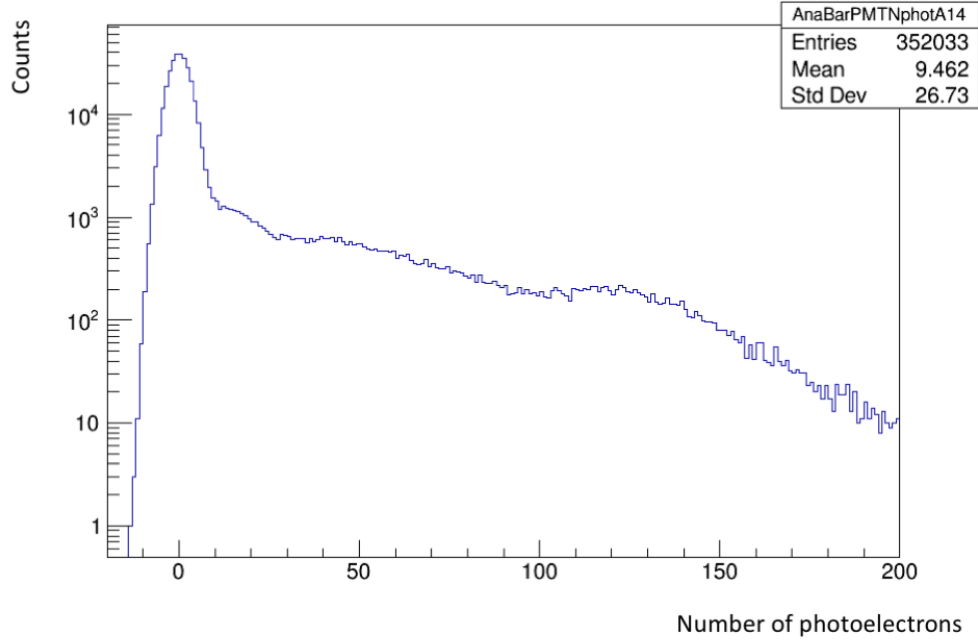


Figure 22: Raw photoelectron number distribution for one paddle/PMT in the simulation

The distribution of energy deposition per primary event is also an important plot. This distribution is for an individual paddle and includes all events that produced a trigger. However, energy deposition data is not recorded per event, but per hit. Therefore, for each event, the analysis code loops through all hits and adds up all the energy deposited in each paddle to obtain the total energy deposition per event in each paddle. When the distribution is plotted for one paddle, as shown in Fig. 23, a large peak is seen around 2 MeV. These events correspond to shallow-angle primaries that only deposit a few MeV in each paddle. A smaller, low peak can also be seen around 7 MeV; these events correspond to near-vertical primaries.

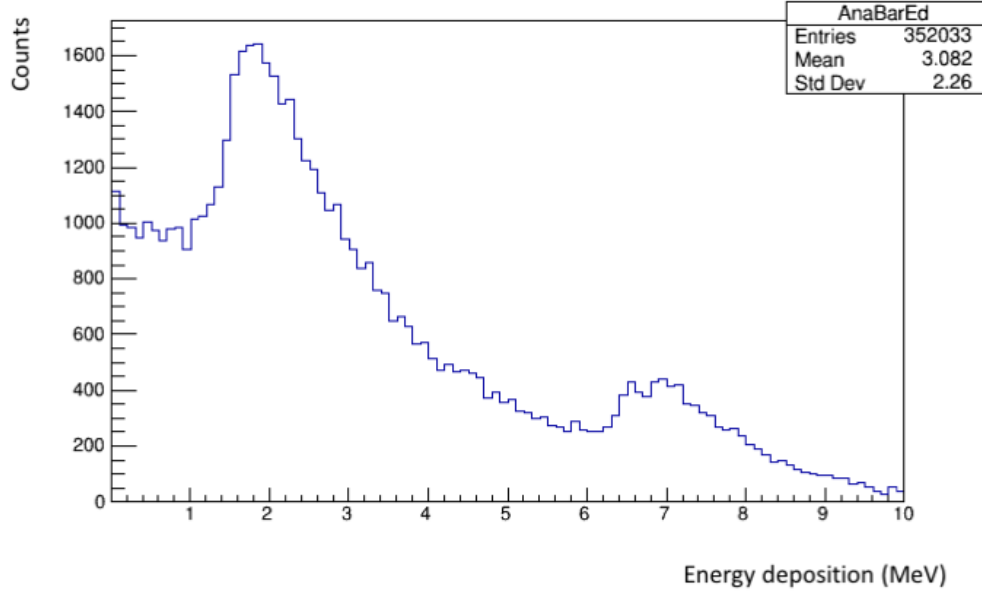


Figure 23: Raw distribution of energy deposition in one paddle in the simulation

The third important piece of simulation analysis is a plot of energy deposition vs. photoelectron number per primary event. This is a two-dimensional histogram, also functioning as a scatter plot, that includes all trigger events in a single paddle. Energy deposition is plotted on the  $y$ -axis, and number of photoelectrons is plotted on the  $x$ -axis. As shown in Fig. 24, the trend is approximately linear, showing that PE number and energy deposition are proportional to each other to first order.

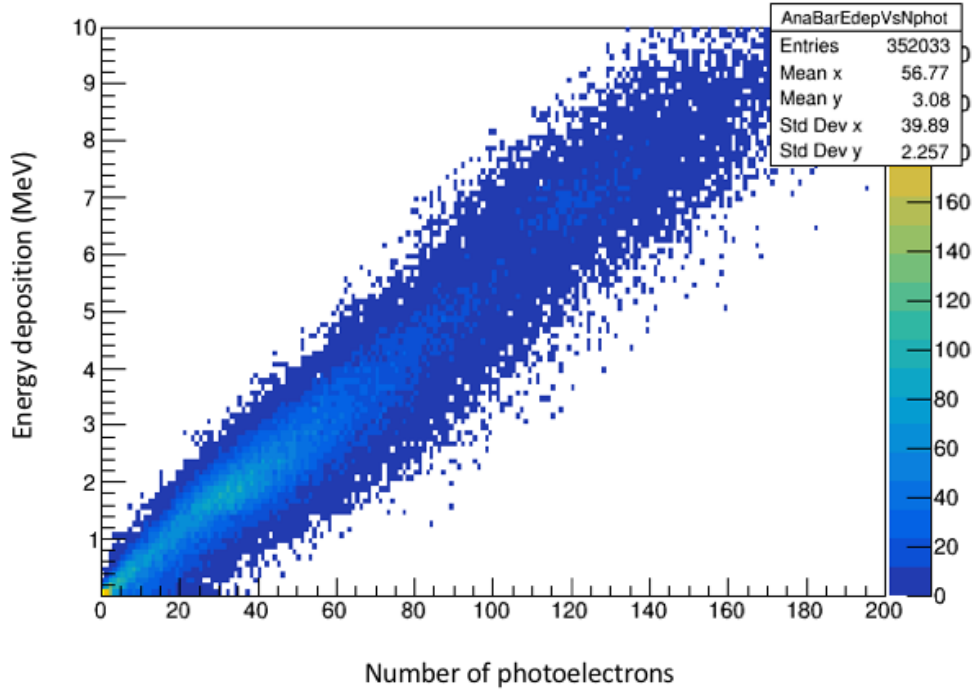


Figure 24: Plot of energy deposition vs. number of photoelectrons per primary event, per paddle. Energy deposition is on the  $y$ -axis in units of MeV; number of photoelectrons produced is on the  $x$ -axis.

### Testing of optical efficiency

In the simulation, the trigger paddle and incident primary region cover about one-fifth the length of the bar. To test the optical efficiency of the bar, the simulation was run five times, with the trigger paddle and primary region shifted up or down over the bar so that the primaries passed through a different section of the bar during each run (Fig. 25). The results of each run were then compared to see if they varied with primary position along the bar, and if so, by how much. The main result compared was the mean number of photoelectrons produced from a single paddle.

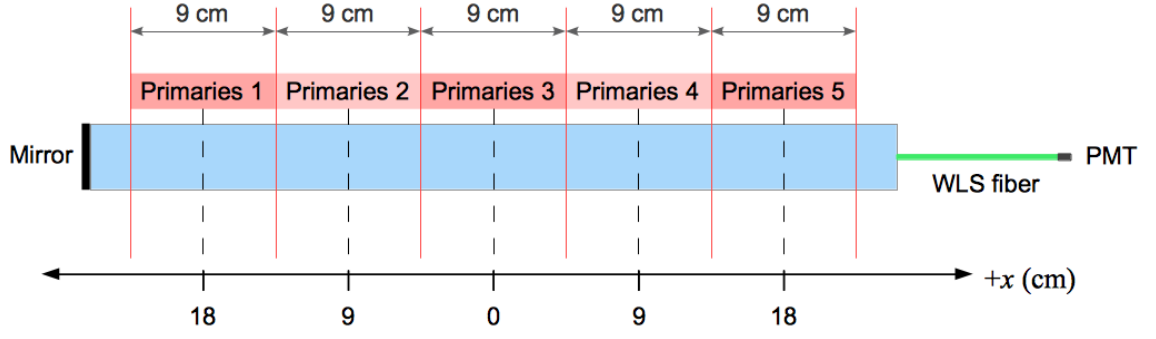


Figure 25: Side-view diagram of bar model showing the five incident primary regions along the bar length used in the five simulation runs. Incident primary regions are indicated by red separating lines. Center coordinate of each region is labeled on the  $x$ -axis.

Next, the simulation was re-run another five times just as before, but with the end mirror removed. The same results (mean PE per paddle) of these five runs were compared to see if there was an increased dependence on the position of the primaries along the bar without the mirror. The results were also compared between the runs with the mirror removed and the runs with the mirror on to measure the effect of the mirror on the efficiency of the bar.

The difference in the optical behavior of the bar with the mirror on vs. off is demonstrated qualitatively in Figs. 26 and 27, which show visualizations of the simulated bar model along with particle tracks in each case. In Fig. 26, in which the mirror is present, photons (green lines) escape from the bar only through the front end around the WLS fibers. (There is also a photon spray emerging from the trigger paddle.) The area around the back end of the bar is dark. In Fig. 27, the mirror is absent, and a significant amount of photon loss (green lines) is seen emerging from the back end of the bar. In both figures, only a few primaries (red lines) pass through the detector.

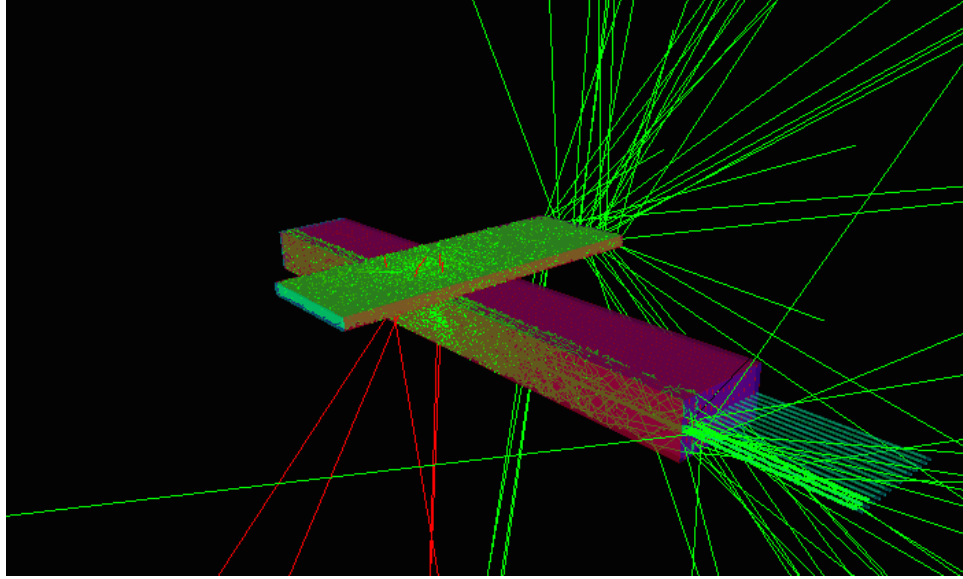


Figure 26: 3D visualization of bar model, with end mirror on. Green lines represent photon tracks; red lines represent primary muon tracks.

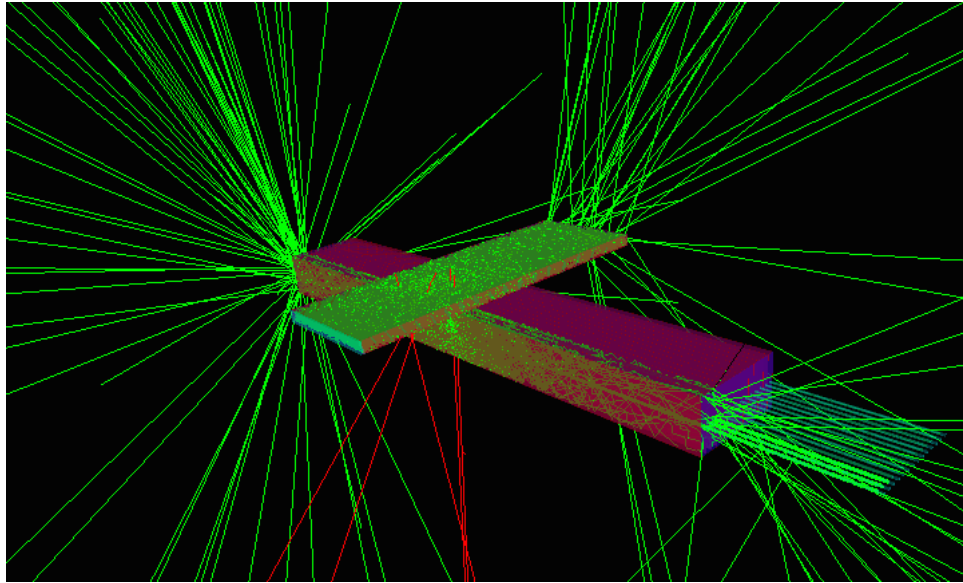


Figure 27: 3D visualization of bar model, end mirror removed. Notice the spray of photons (green lines) out the back end of the bar.

The quantitative results are shown in Figs. 28-30. Figures 28 and 29 show plots of mean photoelectron yield vs. the center position of the trigger paddle and incident primary region over the length of the bar. The photoelectron yield values are normalized to the largest value in each plot such that all values are represented as fractions of the maximum value. As expected, the maximum yield occurs when the primaries strike the bar at the front end, closest to the PMTs, and the minimum yield occurs when the primaries strike the bar at the back end, furthest from the PMTs. In Figs. 28a and 28b, the yield values are normalized to the maximum yield occurring with the mirror on and with the mirror off, respectively; in Fig. 29, the yield values are all normalized to the maximum yield occurring with the mirror on.

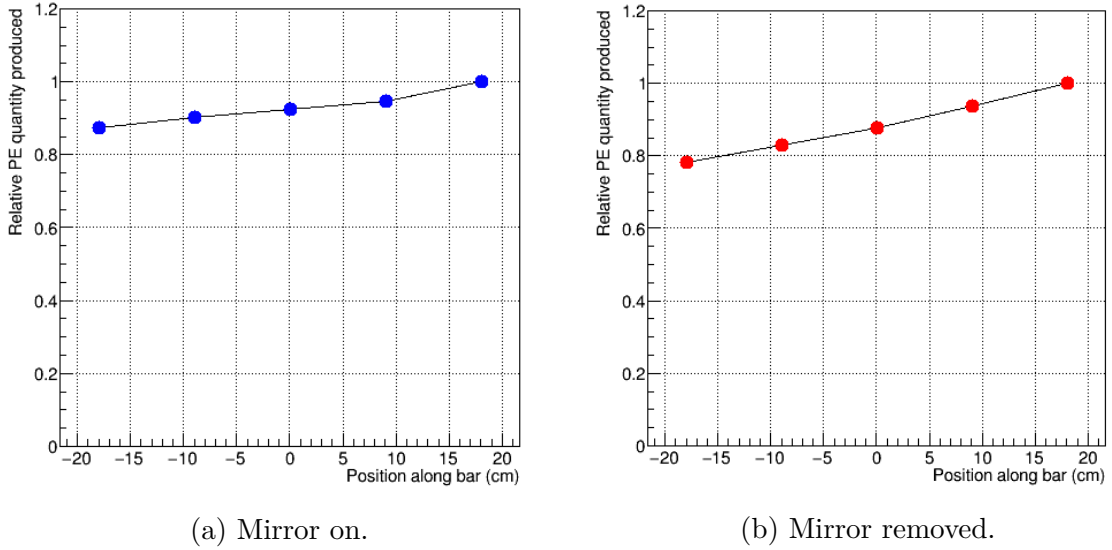


Figure 28: Mean photoelectron yield vs. center position of incident primary region over length of bar. Photoelectron yield values are represented as fractions of the maximum value in each graph. Error bars are inside data points.

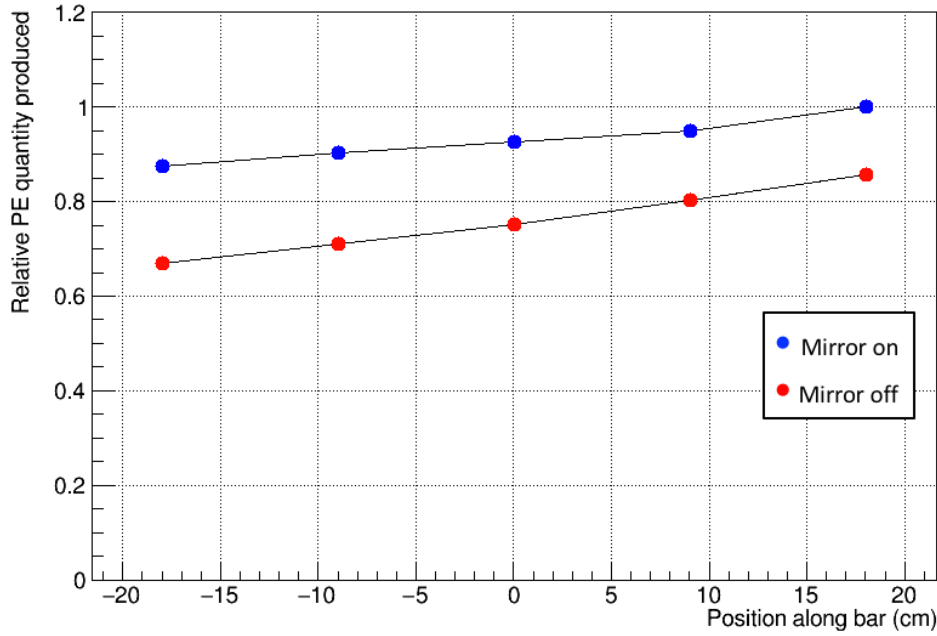


Figure 29: Mean photoelectron yield vs. center position of incident primary region over length of bar. Yield values are represented as fractions of the maximum yield occurring with the mirror on. Error bars are inside data points.

Comparing Fig. 28a to Fig. 28b, the mirror visibly reduces the dependence of the photoelectron yield on the position of the primaries along the bar. Position dependence is not eliminated, but the “slope” is flatter. With the mirror on, the lowest yield value is about 87% of the highest value; without the mirror, the lowest yield value is about 78% of the highest value. Estimating from the endpoints alone, the position dependence is about  $0.0036 \text{ cm}^{-1}$  with the mirror on, while the position dependence is about  $0.0061 \text{ cm}^{-1}$  without the mirror, so the mirror reduces the position dependence by about 41%.

In Fig. 29, the yield data both with and without the mirror are plotted relative to the same maximum value, showing the relative sizes of all the data points. The overall yield is significantly higher over the whole length of the bar with the mirror than without. Of specific note, the lowest yield value with the mirror on is slightly greater than the highest yield value without the mirror.

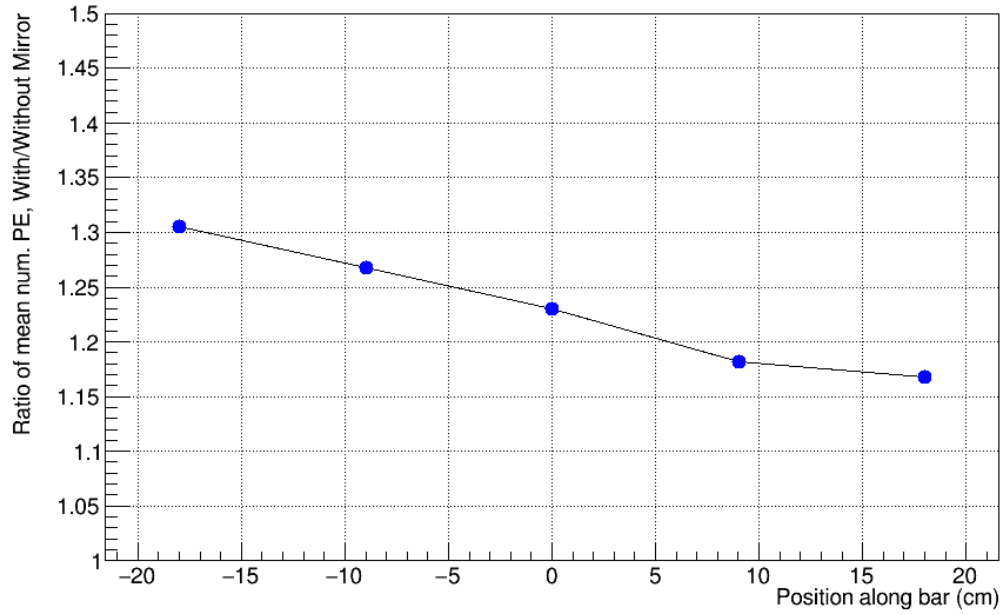


Figure 30: Ratio of photoelectron yield, mirror-on to mirror-off, vs. center position of incident primary region over length of bar. Error bars are inside data points. The lowest value shown on the  $y$ -axis is 1, not 0.

Figure 30 shows the ratio between the mirror-on yield value and the mirror-off yield value at each position. This shows the percent increase in signal resulting from the mirror, relative to the signal without the mirror, at each location. As expected from the previous results, the increase is greatest at the back end of the bar, where the mirror is. This maximum percent increase is about 30.5%. At the front end of the bar, where the increase in signal size is the smallest, the percent increase is about 17%.

In summary, the data shows that the mirror significantly reduces the dependence of the signal size on the incident primary position along the bar, and also significantly increases signal size over the whole length of the bar.



## Calibration of ADC spectra

To perform the ADC calibration analysis, the ADC distributions from the test data and the PE count distributions from the simulation needed to be analyzed together. To achieve this, the ADC distribution analysis and the PE count distribution analysis were copied from the test data analysis code and the simulation analysis code, respectively, and put into a new code for the ADC calibration analysis. In order to easily copy over the photoelectron distribution analysis, however, the simulation analysis code was rearranged first. The simulation analysis code originally produced all groups of plots within the same routine, making it difficult to distinguish which parts of the analysis were needed for the PE distributions and which components were not. To remedy this problem, all plot groups were parsed into separate routines which could be run individually, with all necessary analysis steps duplicated in each routine. The routine to plot the PE distributions was then simply copied into the new ADC calibration code. Except for a couple of analysis routines left in the simulation analysis code, all necessary ADC calibration and crosstalk analysis processes were implemented in this new code.

To calibrate the ADC spectra, the photoelectron distributions from the simulation were fitted to the ADC distributions from the test data, using the energy data from the simulation to relate energy deposition to ADC channel. However, the distributions of PE number could not be fitted directly onto ADC distributions. To allow the simulation data to be fitted to the test data, the ADC distributions from the test data were converted into distributions of photoelectron number. The choice was made to convert ADC to PE number, rather than convert the PE number distributions from the simulation into ADC channels, because the number of photoelectrons produced in the PMT is a direct result of physics. The calibration was then achieved both through proper fitting of the simulation distributions to the converted test data distributions

and through proper conversion of the ADC spectra into photoelectron number spectra.

### ***General procedure***

The method used to convert the test data ADC spectra into PE count spectra is as follows. First, the ratio of PE number to energy deposited is obtained from the plot of energy deposition vs. photoelectron number resulting from the simulation. Then the energy deposited in one paddle by the average vertical primary is obtained from theory (and later verified by the simulation). Multiplying the PE per MeV ratio by the average vertical track energy deposition gives the average photoelectron number produced by a vertical primary. Dividing the average vertical track PE yield by the mean vertical track ADC channel gives the conversion factor of PE number per ADC channel. This conversion factor is computed for each individual pixel in the test data, since the vertical track ADC distributions do not have the same mean across all paddles/pixels. Then, each ADC spectrum (pedestal included) is converted into a spectrum of PE number. The converted spectra are plotted and fitted in the same way as the ADC distributions, with a Gaussian function on each vertical track peak and pedestal. The fit parameters are extracted for verification analysis and for comparison with the simulation data.

To fit the simulated PE distributions to the converted test data distributions, the ADC neighbor cut is first converted into a PE number cut using the mean PE per ADC conversion factor, which is obtained using the average value of the mean vertical-track ADC channel. The PE count neighbor cut is then imposed on the simulation data in the same manner as on the ADC data. Gaussian fits are applied to the resulting vertical track peaks and pedestals of the simulated PE count distributions. The fit parameters are also extracted for verification analysis and for comparison with the converted test data distributions.

The set of test data used in the entire calibration analysis was taken from PMT 7 on the right side of CDet Module 1. This data set consisted of approximately 500,000 trigger events. Several sets of simulation data were used over the course of the calibration analysis. In all of them, the trigger paddle was positioned in the center of the model CDet bar, as the trigger paddles are always in the center of the real bars in the test setup.

### ***Initial testing***

The initial round of calibration analysis used a simulated data set of 200,000 total events. The ratio of PE number per MeV of energy deposited was estimated by looking at the plot of energy deposition vs. photoelectron number from the simulation analysis. The energy deposition of minimum ionizing particles through the scintillator was estimated to be about 2 MeV per centimeter of thickness [29], so the initial estimate for the energy deposition of vertical primaries was 8 MeV. The initial neighbor cut was about one standard deviation of the pedestal.

The initial results were reasonable; the photoelectron number distributions from the simulation and the converted test data were reasonably similar in shape. This confirmed the appropriateness of the general method used to convert the ADC test data and fit the simulated photoelectron data to the converted test data.

### ***Major modifications and troubleshooting***

After the initial round of analysis, it was discovered that two of the detector material parameters in the Geant4 simulation were incorrect. The search for the problem was prompted by plots of the fit resolutions on the vertical track peaks of the photoelectron number distributions, which showed that the resolutions from the simulation were worse than the resolutions from the real data. As discussed in Chapter III, the photon yield of the scintillator plastic should be 500 photons/MeV, and the quantum

efficiency of the PMT surfaces should be 0.13. However, the photon yield had been specified as 50 photons/MeV, and the quantum efficiency had been specified as 0.24, resulting in an overall signal that was about five times too small. These two parameters were corrected in the Geant4 code, and the simulation was run again to produce a new set of 200,000 events.

The signal sizes in the new simulated data were significantly greater than the signal sizes in the initial simulated data. However, the vertical track peak all but vanished in most of the PE number distributions. This prompted the discovery of two additional problems. First, the quantity of simulation data was insufficient to reasonably compare with the test data. The test data had 500,000 trigger events, while the current simulated data set had only 130,000 trigger events out of the total 200,000. The number  $N$  of simulated events required for comparability with the test data was estimated by taking the ratio of the number of total events to the number of trigger events in the current simulated data set and multiplying that ratio by the number of trigger events in the test data set. The result is given in the following equation.

$$N = \frac{200,000}{130,000} \times 500,000 \approx 769,000 \quad (2)$$

Therefore, the simulation was re-run in 80 batches of 9600 events, resulting in a new total data set of 768,000 events. This data set was used for the rest of the analysis.

The second problem discovered was the size of the neighbor cut. Originally, the ADC neighbor cut had a value of 10 in the test data analysis code, but this value had not been tested to determine whether it was optimal. It was decided that an appropriate neighbor cut value would be three standard deviations of the pedestal; this would allow pedestal noise to be present in the neighboring paddles, but not larger signals. The average value of three standard deviations of the ADC pedestal was computed and found to be about 33 ADC channels. Therefore, the ADC neighbor cut was

increased to 33. The new cut value was then converted to a number of photoelectrons, rounded up to the nearest integer, and applied to the simulation distributions. With this change, the vertical track peak became visible again, as the cut was no longer prohibiting data points for which signals within the pedestal region were present in the neighboring paddles. After the increase in the neighbor cut, the resolutions on the simulated vertical track peaks also became better than the resolutions on the real data vertical track peaks. The value of the PE neighbor cut is 8 photoelectrons.

Another important modification to the analysis was the implementation of a restriction on the trigger condition in the simulation analysis to compensate for the mismatch between the trigger geometry in the simulation model and in the real CDet test setup. In the test setup, the size and placement of the top and bottom trigger paddles impose an angular restriction on the events that cause a trigger. This restriction was modeled in the simulation analysis by adding a cut on the primary momentum polar angle,  $\theta$ , to the trigger condition as follows. The cross-sectional geometry of the test setup is shown in Fig. 31 with a primary passing through opposite edges of the top and bottom trigger scintillators. The polar angle  $\theta$  of this primary is shown as  $\theta_{min}$  in the figure ( $\theta = \pi$  for a vertical primary). Any primary coming in at an angle less than  $\theta_{min}$  will not cause a trigger because it will not pass through both top and bottom trigger scintillators.

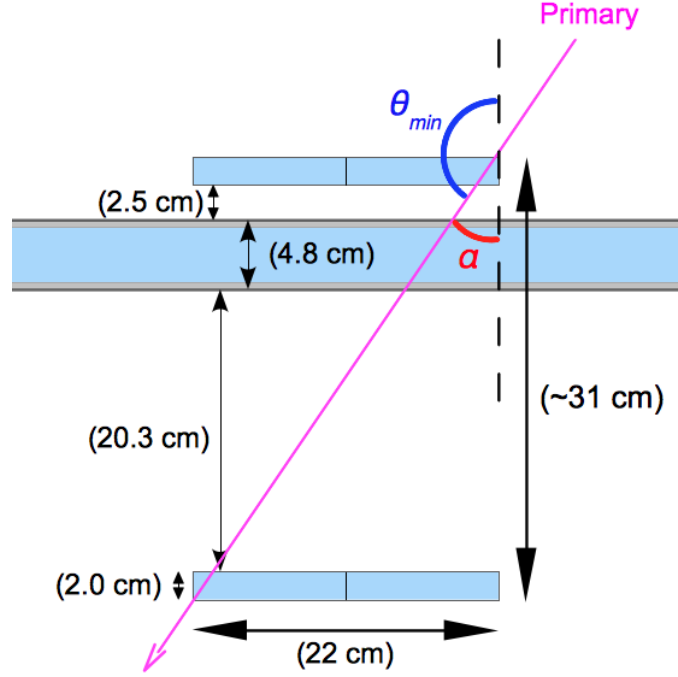


Figure 31: Diagram of trigger paddle geometry in CDet test setup

The supplement of  $\theta_{min}$ ,  $\alpha$  (shown in red), is given by

$$\alpha = \tan^{-1} \frac{\Delta x}{\Delta y}, \quad (3)$$

where  $\Delta x$  is the width of the trigger scintillators and  $\Delta y$  is the height of the entire test setup. The trigger scintillators are 22 cm wide, and the test setup is about 31 cm tall, so

$$\alpha = \tan^{-1} \left( \frac{22}{31} \right) = 0.6172 \text{ rad.} \quad (4)$$

Finally,

$$\theta_{min} = \pi - \alpha \quad (5)$$

$$\theta_{min} = 2.524 \text{ rad.} \quad (6)$$

The value of  $\theta_{min}$  in Eq. 6 was added to the trigger condition as the minimum allowed value of the primary  $\theta$  for trigger events. When each event is read, if a hit is present in both the trigger paddle and one of the paddles in the bar, the primary  $\theta$  value is compared to  $\theta_{min}$ . If  $\theta > \theta_{min}$ , a trigger is considered to have occurred and that event is analyzed; otherwise, a trigger did not occur, and that event is ignored.

The cut placed on the primary  $\theta$  is a two-dimensional approximation of a three-dimensional system. To verify that  $\theta_{min}$  does not cut out any good data, a histogram plot was created showing two versions of the primary  $\theta$ -distribution without the cut imposed (Fig. 32). The large distribution is of all trigger events, and the small distribution is only of events with signals greater than the pedestal. As seen in Fig. 33, which zooms in on the plot in Fig. 32, the  $\theta$ -distribution for events with above-noise signals approximately vanishes around  $\theta = \theta_{min} = 2.524$  radians. Therefore, the  $\theta_{min}$  cut does not cut out good data; instead, it serves to eliminate excess trigger events.

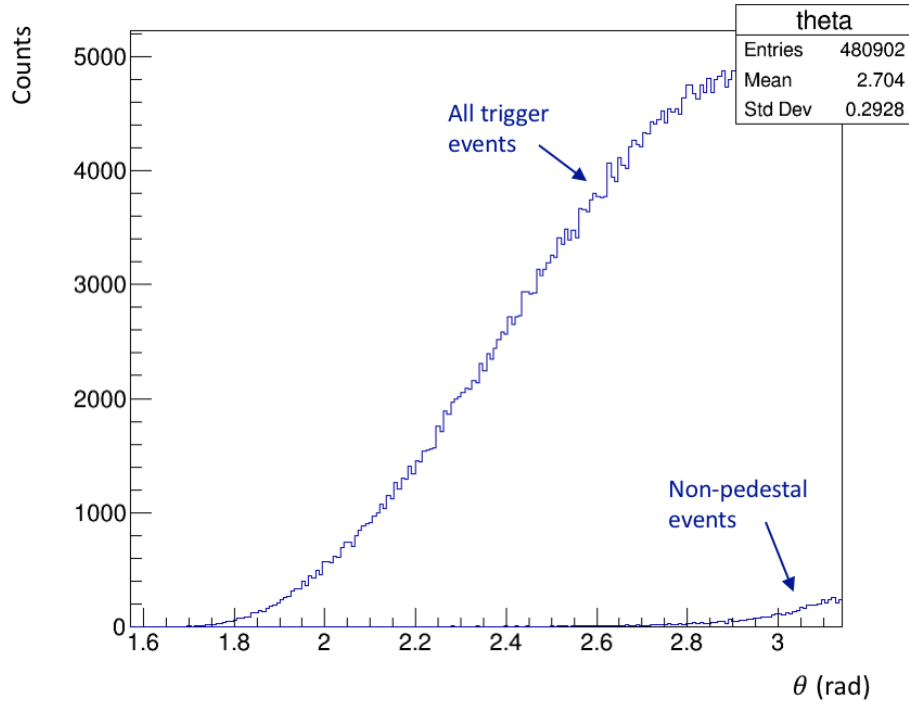


Figure 32: Distribution of primary  $\theta$  without cut

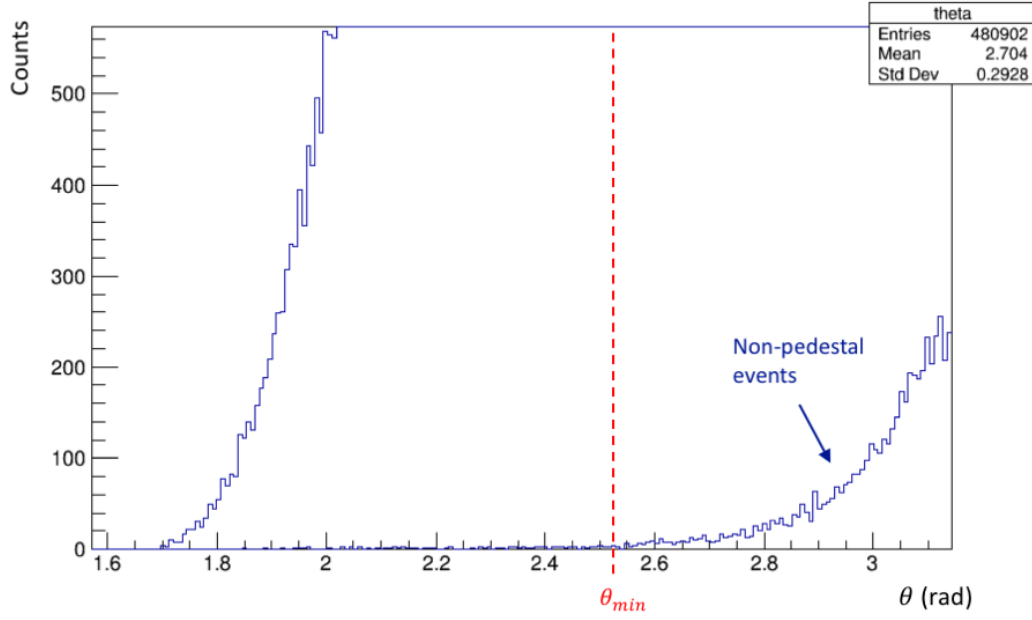


Figure 33: Distribution of primary  $\theta$  without cut for non-pedestal events

### *Final analysis and results*

Several important refinements were made to achieve the final calibration. First, the two-dimensional histogram of energy deposition vs. photoelectron number from the simulation (Fig. 24) was profiled along the  $x$ -axis, converting it into a condensed, conventional scatter plot. The profile plot was then fitted with a linear function to obtain a more accurate ratio of photoelectrons per MeV (PE/MeV). The fitted profile plot is shown in Fig. 34. Since the slope of the fit is for energy vs. PE count and not PE count vs. energy, the reciprocal of the slope was taken to obtain the PE/MeV ratio.



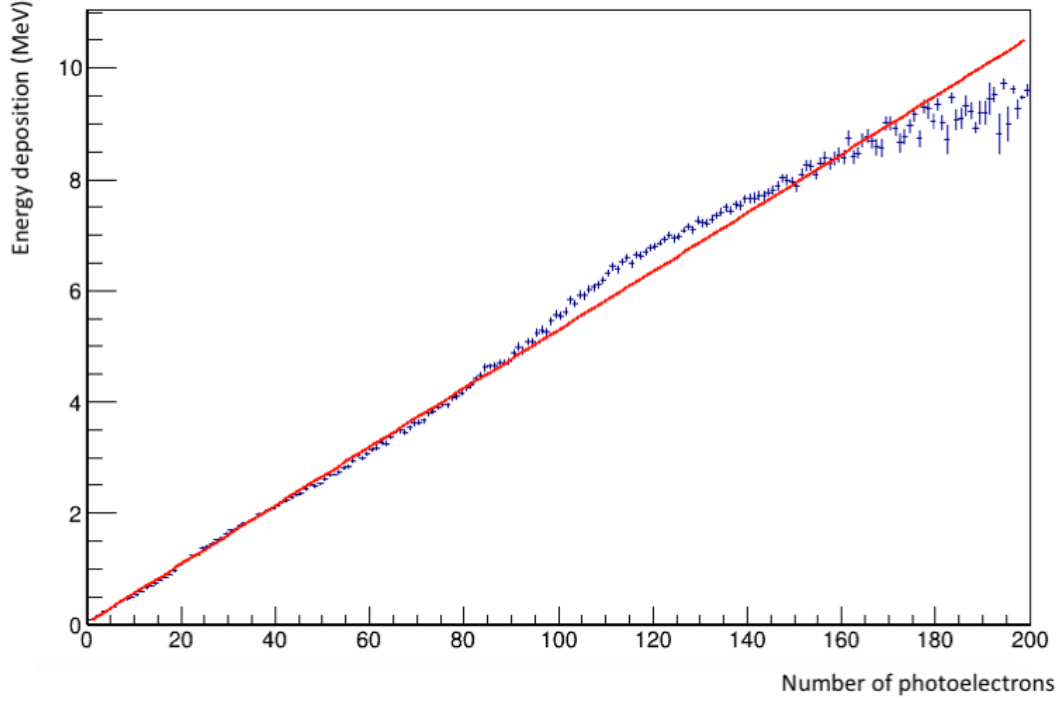


Figure 34: Profile of energy deposition vs. photoelectron number 2D histogram, with linear fit.

The slope of the fit line is  $(0.0525775 \pm 4.55 \times 10^{-5})$  MeV/PE. The ratio of photoelectrons per MeV of energy deposited is  $(19.02 \pm 0.016)$  PE/MeV.

Next, the mean vertical track energy deposition was calculated from the simulation and then verified against theory. The energy deposition distributions were plotted for all 14 paddles. The vertical track peaks were fitted and the average mean energy deposition computed. In order to restrict the energy deposition distributions to near-vertical primaries only, a minimum cut was placed on the primary  $\theta$  value. After some trial and error, a minimum cut of  $\theta = 3.05$  was chosen. The near-vertical track energy deposition distribution from one paddle is shown in Fig. 35.

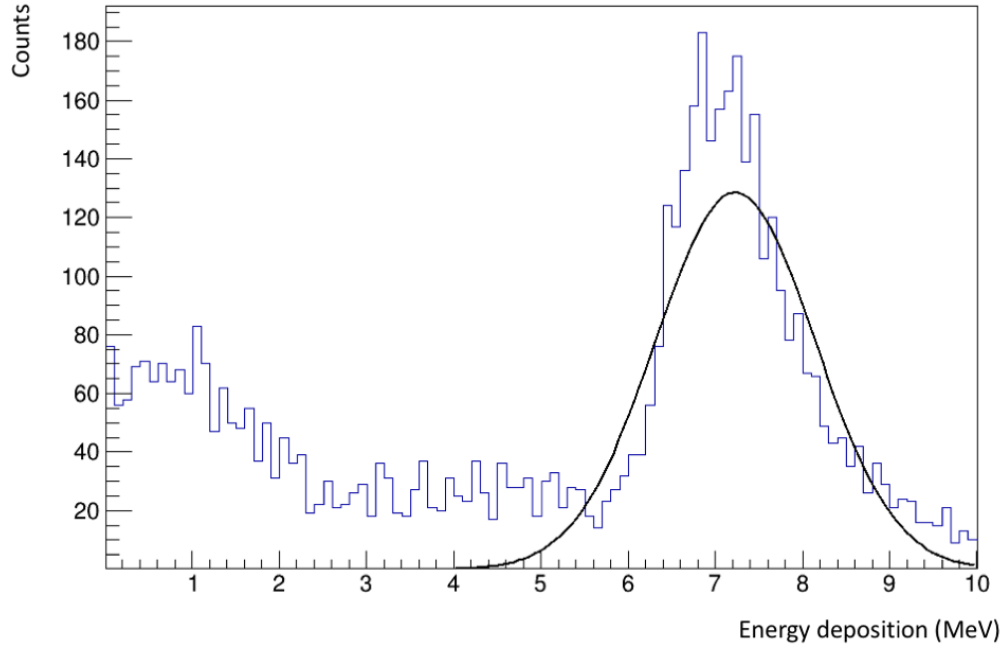


Figure 35: Energy deposition distribution of near-vertical primary muons in one paddle. The polar angle  $\theta$  is restricted to the range  $3.05 \leq \theta \leq \pi$ .

The average mean vertical track energy deposition was found to be  $(7.239 \pm 0.005)$  MeV. This number was rounded to 7.24 for the calculation of the ADC-to-PE conversion factors. According to theory [30], the energy deposition of minimum ionizing muons in plastic scintillator should be about 1.8 to 1.84 MeV per centimeter of thickness traversed, which means that the energy deposited in the CDet paddles by near-vertical primaries should be about  $1.8 \text{ MeV/cm} \times 4 \text{ cm} = 7.2 \text{ MeV}$  to  $1.84 \text{ MeV/cm} \times 4 \text{ cm} = 7.36 \text{ MeV}$ . The mean energy deposition value obtained from the simulation is consistent with this.

An additional parameter was also added to the ADC conversion factor to correct for an overall systematic error. The vertical track peaks in the PE number distributions from the converted test data consistently had higher means than those in the simulated

data distributions. In the original ADC-to-PE conversion factor,

$$\text{PE/ADC} = \frac{(\text{PE/MeV}) * (\text{Avg. Mean Energy Deposited})}{(\text{Mean ADC})}, \quad (7)$$

the numerator was assumed to represent the mean photoelectron yield from vertical track primaries. However, the value of the numerator turned out to be higher than the means of the vertical track peaks in the simulated PE distributions, making the ADC conversion factor too large. The reason for this discrepancy is not entirely known; however, it may result from the fact that the relation between energy deposition and photoelectron yield is not perfectly linear. In Fig. 34, the data points deviate significantly from the linear fit in the region from about 100 to 140 photoelectrons. In this region, the data indicate a slightly lower ratio of photoelectrons per MeV than the fit line, the inverse slope of which provides the PE/MeV parameter. The mean photoelectron yield for vertical tracks (see Figs. 36 and 37) lies within this region. Therefore, the difference between the energy deposition vs. photoelectron count data and the linear fit may contribute to the difference between the numerator of Eq. 7 and the mean values of the simulated vertical track peaks. To correct for this systematic error, a so-called “efficiency parameter” was added as follows:

$$\text{PE/ADC} = \frac{(\text{PE/MeV}) * (\text{Avg. Mean Edep}) * (\text{Efficiency parameter})}{(\text{Mean ADC})}, \quad (8)$$

where “Edep” stands for energy deposited. The value of the efficiency parameter was initially estimated by taking the average mean PE count from the simulation distributions and dividing that by the numerator of Eq. 7. It was then refined by trial and error, and was finally chosen to be

$$\text{Eff.} = 0.84 \pm 0.01 . \quad (9)$$

The final photoelectron number distributions are shown in Figs. 36 and 37. The simulated distributions are fitted to the converted test data distributions and are displayed one on top of the other. Figure 36 shows the distribution plot for one paddle, enlarged for readability, while Fig. 37 shows the distribution plots for all paddles. The vertical track peaks are all of similar size, shape, and position, and neither data set has systematically higher or lower means than the other. The mean photoelectron yield for vertical tracks is about 117 photoelectrons.

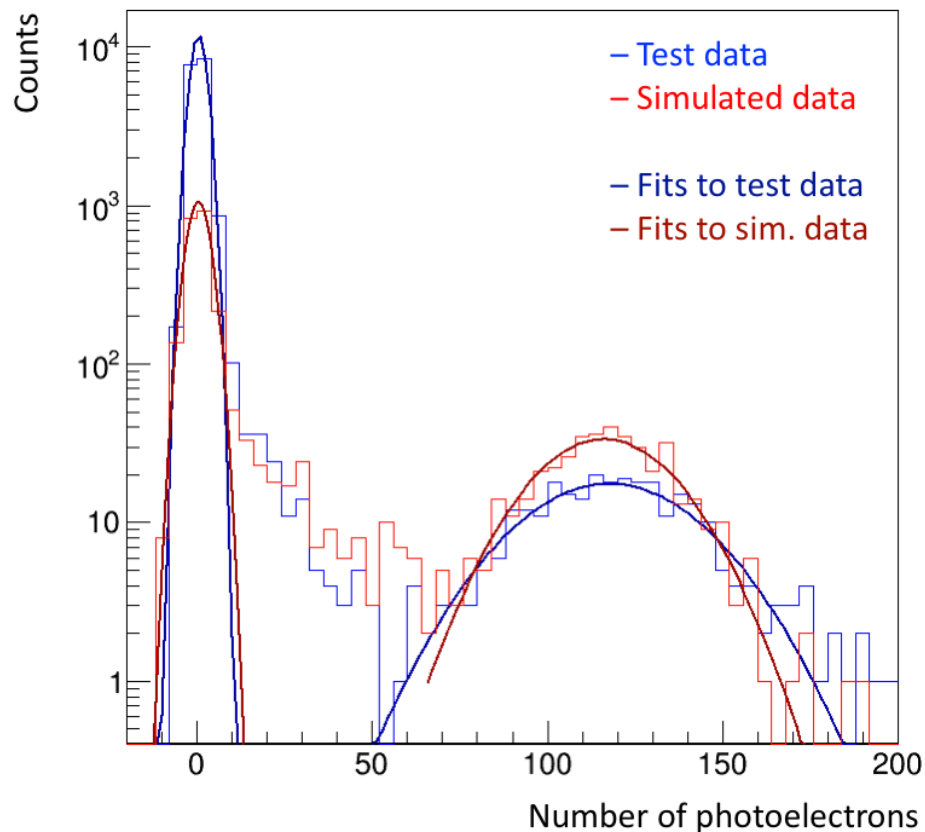


Figure 36: Overlaid distributions of photoelectron number from test data and simulation for one paddle. Dark blue curves are Gaussian fits to the peaks in the test data. Dark red curves are Gaussian fits to the peaks in the simulated data.

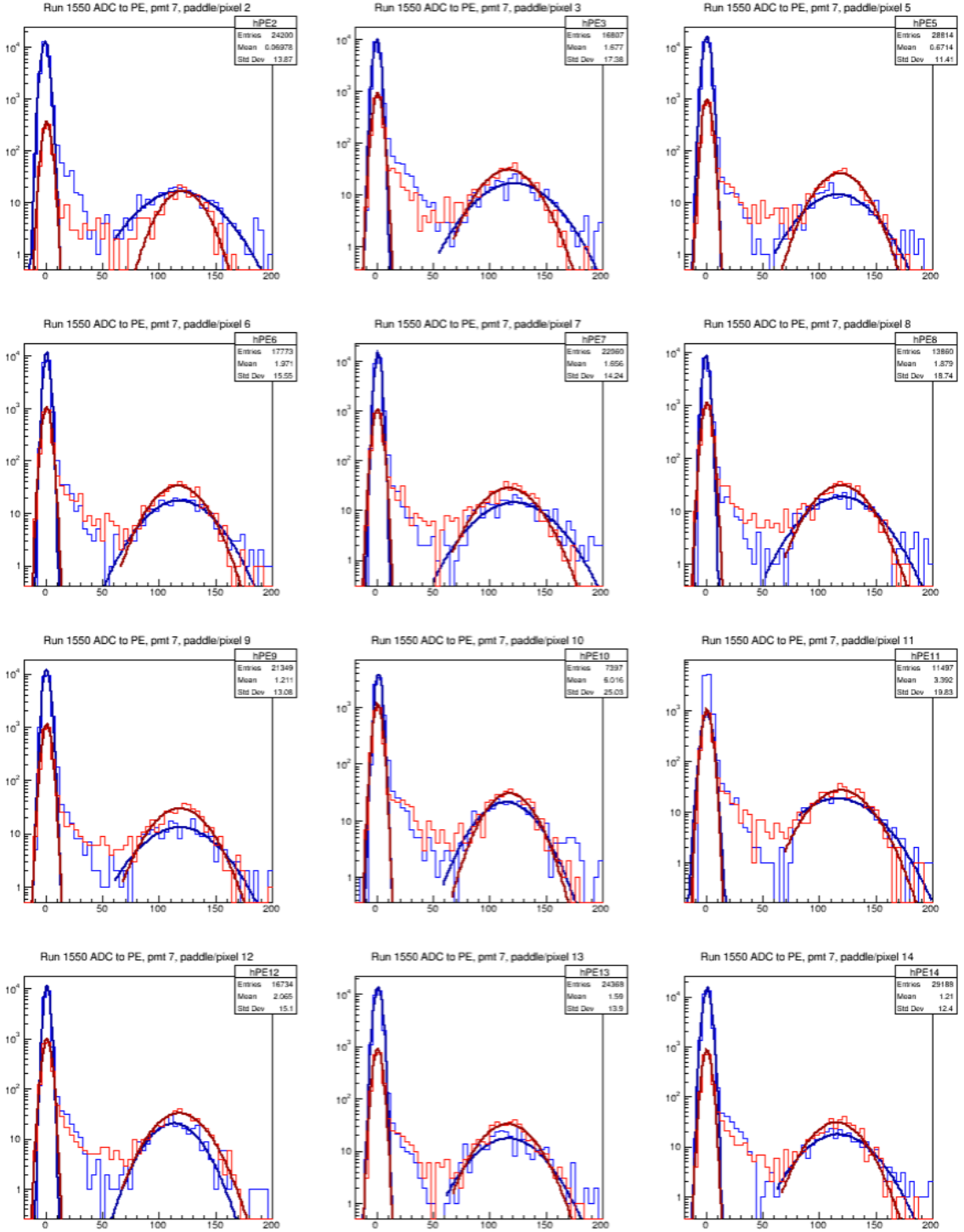


Figure 37: Photoelectron number distribution plots for all paddles analyzed. Blue curves are Gaussian fits on test data peaks (blue histograms); red curves are Gaussian fits on simulated data peaks (red histograms). Axes are the same as in Fig. 36.

There are only 12 plots in Fig. 37 instead of 14 because the outer two paddles of the simulated bar, #1 and #14, are omitted from the analysis. This is because these two paddles have only one neighbor paddle each. Bar #7 in the real CDet module is flanked by two other bars, so the outer two paddles still have neighbors on both sides. However, when the neighbor cut is applied to the outer two paddles in the simulation, the spectrum is misshapen because there is only one neighbor paddle to compare with and not two. This was confirmed by altering the analysis of the test data slightly such that for paddles #1 and #14 of the real bar, the neighbor cut condition would ignore the neighbor paddle in the adjacent bar and only check the neighbor paddle within the same bar. As shown in Fig. 38, the resulting distributions for the outer two paddles from the test data have a similar appearance to the corresponding distributions from the simulation.

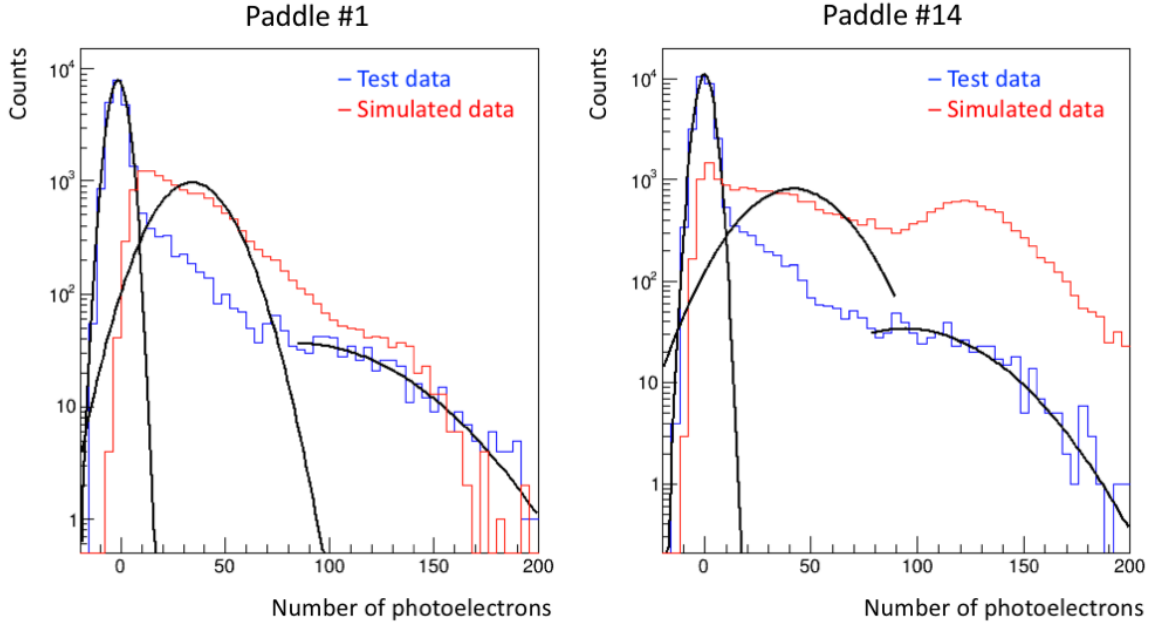


Figure 38: Distributions of photoelectron number in the outer two paddles of the bar, when the neighbor cut is only applied to one neighboring paddle and not two.

Table 2 lists all the important parameters used in the final calibration analysis. The standard deviation of the smearing function used to reproduce the pedestal in the simulated data was chosen by way of approximation. The original estimate in the simulation analysis code was  $\sigma = 3$ , as the width of the resulting pedestal peak appeared proportionally similar to the width of the pedestal in the ADC distributions. During the final phase of the calibration analysis, the standard deviation was adjusted to  $\sigma = 2.9$  to slightly improve the fit of the simulated photoelectron number distributions to the converted test data distributions. As seen in Figs. 36 and 37, the value of  $\sigma = 2.9$  produces pedestals in the simulated PE distributions that match those in the converted test data quite closely.

Table 2: Final ADC calibration analysis parameters

Photoelectrons per MeV	$(19.02 \pm 0.016)$ PE/MeV
Avg. mean energy deposition of vertical primaries	$(7.24 \pm 0.005)$ MeV
Efficiency parameter	$0.84 \pm 0.01$
Std. dev. for pedestal smearing of simulated data	2.9
PE number neighbor cut	8
ADC neighbor cut	33
PE number histogram bin size	4
“Good” TDC interval for test data	850 – 950

The TDC interval, used for the initial cut on the ADC test data, was simply read from plots of the raw TDC distributions in the test data. In the original test data analysis code, the TDC interval was specified as 900 – 950, which did not include all events in the pedestal; the interval was widened in the calibration analysis to include all pedestal events.

Two sets of plots are used to verify the overall accuracy of the final vertical track distributions. First, the resolutions of the fits on the vertical track peaks are plotted for the simulated photoelectron count data and for the converted test data, shown in Fig. 39. The resolution of a peak is defined as the standard deviation divided by the mean; the narrower the peak, the better the resolution and the smaller the resolution value. Both of these plots show that the vertical track peaks have reasonably good resolutions. Also, the resolutions on the simulated data are better than the resolutions on the test data, as expected for an idealized simulation.

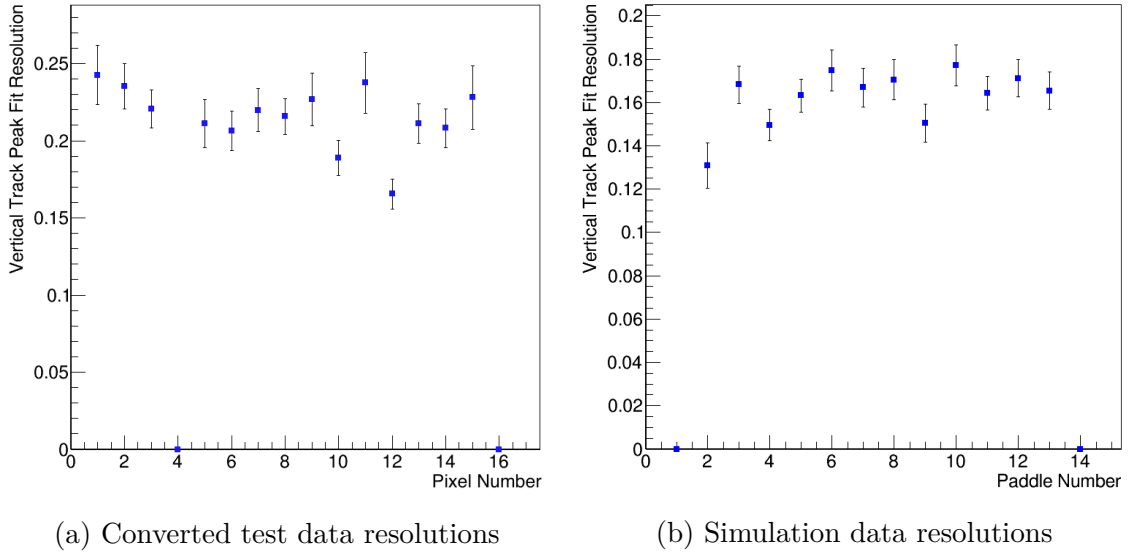


Figure 39: Resolutions of the fits on the vertical track peaks in the photoelectron number distributions.

The second set of plots shows the approximate number of data points in each vertical track peak in the photoelectron number distributions. The data counts for the converted test data and the simulation data are shown in Figs. 40a and 40b, respectively. As seen in the figures, the average data count in the vertical track peaks in the real data is about 1100, and the average count in the simulated vertical track peaks is about 1500. The simulated data counts are slightly higher than the test data counts;



however, the sizes of the peaks are reasonably comparable between the test data and the simulated data. This confirms that the quantity of simulated data used was appropriate for the size of the test data set. The reason for the unusually small value of the leftmost data point in Fig. 40b, corresponding to paddle #2 in the simulation, is unknown. However, it seems to have caused no adverse effects in the analysis.

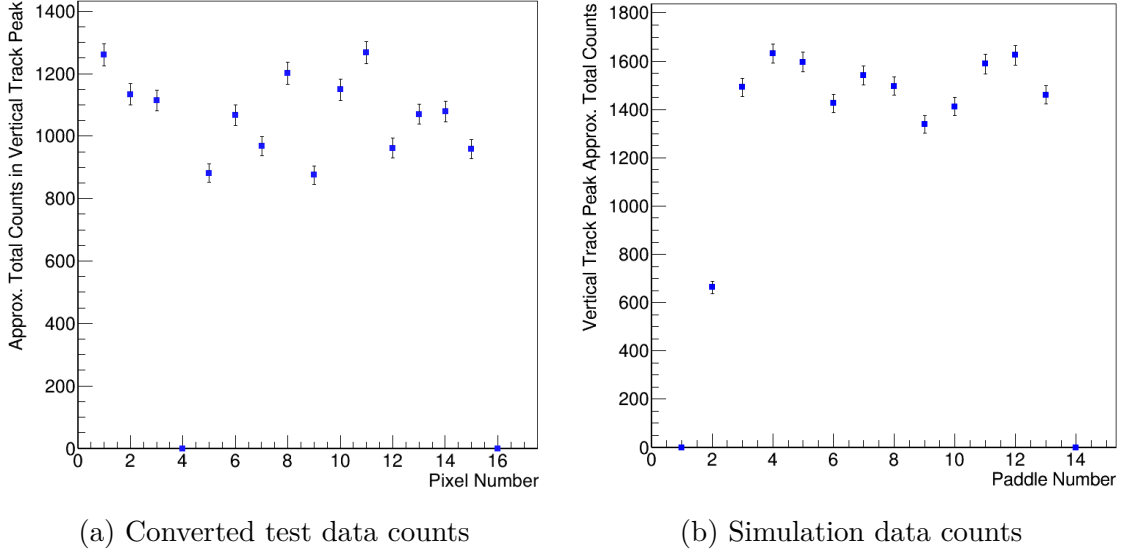


Figure 40: Approximate data counts in the vertical track peaks in the photoelectron number distributions

The overall accuracy of the calibration analysis having been verified, the calibration results are as follows. The final ADC-to-PE conversion factor, given in Eq. 8, is repeated below.

$$\text{PE/ADC} = \frac{(\text{PE/MeV}) * (\text{Avg. Mean Edep}) * (\text{Efficiency parameter})}{(\text{Mean ADC})} \quad (10)$$

To obtain the conversion between ADC channel and energy deposition, the number of photoelectrons per ADC channel (PE/ADC) should be divided by the number of

photoelectrons per MeV of energy deposited (PE/MeV), resulting in

$$\text{Edep/ADC} = \frac{(\text{Avg. Mean Edep}) * (\text{Efficiency parameter})}{(\text{Mean ADC})}. \quad (11)$$

However, the correction from the efficiency parameter applies to the overall result of processes within the simulated detector, not to the amount of energy deposited. Therefore, the efficiency parameter must be divided out as well, giving

$$\text{Edep/ADC} = \frac{\text{Avg. Mean Edep}}{\text{Mean ADC}}. \quad (12)$$

The ADC spectra are meant to be calibrated per pixel, so “Mean ADC” in Eq. 12 will be the mean of the vertical track peak in each individual ADC distribution. Referencing Tab. 2, “Avg. Mean Edep” is equal to 7.24 MeV. The final ADC calibration factor, including the uncertainty from the two preceding division operations, is given by

$$\text{Edep/ADC} = \frac{(7.24 \pm 0.12) \text{ MeV}}{\text{Mean ADC}}. \quad (13)$$

As an additional result, the ratio between photoelectron yield and energy deposited is important for the full Geant4 simulation of SBS that is being used for the commissioning of the entire spectrometer. This simulation is so large that optical photon tracking is not computationally feasible. The ratio of photoelectron yield to energy deposited is a necessary conversion factor to accurately simulate photoelectron output from CDet based directly on energy deposited in the detector. The PE-to-energy conversion factor,  $P$ , is computed as

$$P = \frac{\langle PE \rangle}{\langle \text{Edep} \rangle}, \quad (14)$$

where  $\langle PE \rangle$  is the average mean vertical track photoelectron yield and  $\langle \text{Edep} \rangle$  is the

average mean vertical track energy deposition. The average mean photoelectron yield is

$$\langle PE \rangle \approx 117 \pm 0.59, \quad (15)$$

where the uncertainty in the mean is estimated from the plots in Fig. 37. The average mean energy deposition is given by

$$\langle E_{\text{dep}} \rangle = (7.24 \pm 0.12) \text{ MeV}, \quad (16)$$

as in the numerator of Eq. 13, to include the uncertainty associated with the test data and not the CDet simulation only. Therefore, the conversion factor from energy deposition to photoelectron number is

$$P = (16.2 \pm 0.28) \text{ PE/MeV}. \quad (17)$$

### **Crosstalk analysis**

In PMT 7, in the right half of CDet Module 1, pixels 4 and 16 are not used, and the 14 paddles in the corresponding scintillator bar are connected in order as shown in the pixel map in Fig. 41. As a result, there are ten pairs of adjacent pixels with non-adjacent paddles (e.g. pixels 1 and 5), and ten pairs of adjacent pixels that are connected to adjacent paddles (e.g. pixels 1 and 2). To test the level of crosstalk between pixels, two sets of plots were created to compare the signals in each pair of pixels: one set using the ADC test data, and the other set using the test data converted into numbers of photoelectrons. Each set consists of ten plots for the pixel pairs with non-adjacent paddles and ten plots for the pairs with adjacent paddles. Each plot is a two-dimensional histogram with the signal in one pixel (referred to as pixel A) on the  $x$ -axis and the signal in the other pixel (referred to as pixel B) on the

$y$ -axis. Because neighbor paddles are being compared, only the TDC cut is used on the data and not the neighbor cut. For each event, if the ADC signal in pixel A is greater than 50 ADC channels, meaning the signal is definitely above the pedestal, then the signal is added to the  $x$ -dimension of the histogram, and the signal in pixel B, whatever the size, is added to the  $y$ -dimension; this condition applies for both the ADC plots and the converted PE number plots.

<b>1</b> <b>1</b>	<b>2</b> <b>2</b>	<b>3</b> <b>3</b>	
<b>5</b> <b>4</b>	<b>6</b> <b>5</b>	<b>7</b> <b>6</b>	<b>8</b> <b>7</b>
<b>9</b> <b>8</b>	<b>10</b> <b>9</b>	<b>11</b> <b>10</b>	<b>12</b> <b>11</b>
<b>13</b> <b>12</b>	<b>14</b> <b>13</b>	<b>15</b> <b>14</b>	

**Pixel number (black)**  
**Paddle number (red)**

Figure 41: Map of maPMT pixels and connected paddle fibers for PMT 7 in CDet Module 1, right half

For comparison, a third set of plots was created in the same manner using the simulated PE number data, with ten plots for non-adjacent paddle pairs and ten plots for adjacent paddle pairs; for non-adjacent paddle pairs, the plots are expected to show no correlation at all between the signals. To include only signals from paddle A that are above the pedestal region, the PE neighbor cut value of 8 photoelectrons was used as the minimum signal size condition.

All ten plots in each subset are essentially identical in appearance; one example of each is shown in each of the following figures. Only the plots of the test data converted to numbers of photoelectrons are shown in order to best compare with the plots of the simulated data. The test data plots are shown in Figs. 42 and 44, and the simulated data plots are shown in Figs. 43 and 45. The plots for non-adjacent paddles are in Figs. 42 and 43, and the plots for adjacent paddles are in Figs. 44 and 45.

Figure 42, which compares the test data between non-adjacent paddles, shows no evidence of significant crosstalk. The signals from the two pixels are clearly not correlated. When a large signal is present in pixel A, a signal of any significant size is unlikely to be present in pixel B. The overall form of the distribution is very similar to Fig. 43, which shows the uncorrelated signals from two non-adjacent paddles in the simulation. In both figures, most of the signals in pixel/paddle B are in the pedestal. A statistical fringe is present on the upper “hypotenuse” of the distribution. The larger number of signals in the lower left corner of each plot may be the result of shallow-angle primaries that passed through several paddles, depositing some energy in each.

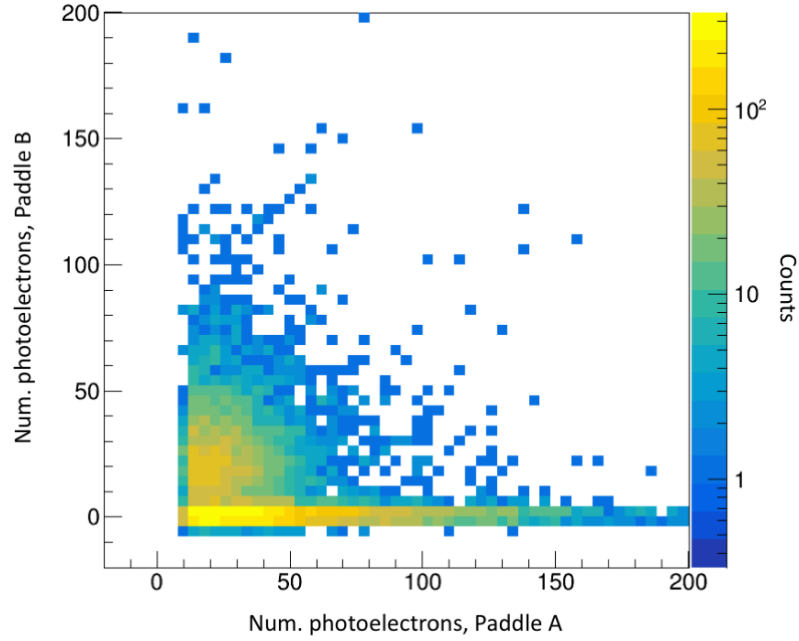


Figure 42: 2-D histogram showing PE signal in one pixel vs. PE signal in adjacent pixel with non-adjacent paddle for test data. Signal values along  $x$ -axis are all above the pedestal. Data counts are shown by color scale.

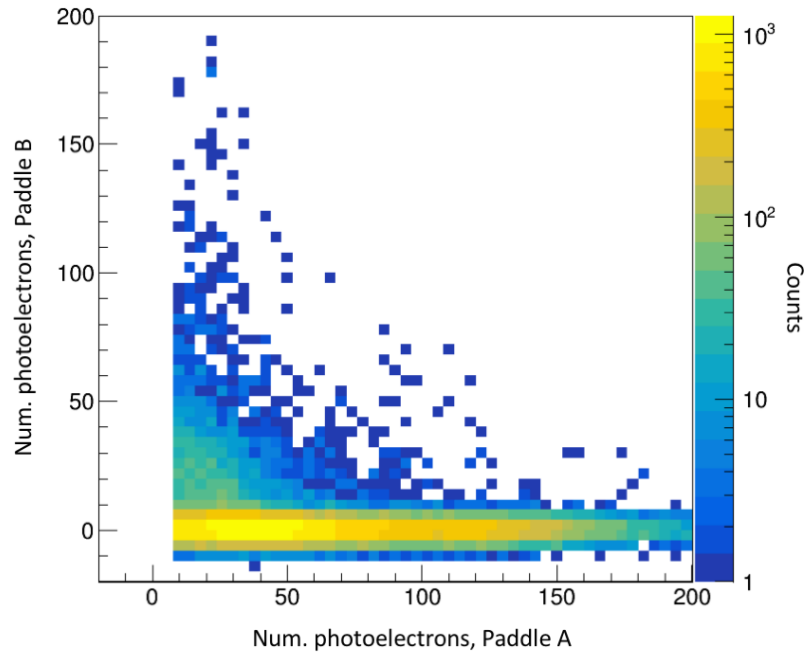


Figure 43: 2-D histogram showing PE signal in one paddle vs. PE signal in non-adjacent paddle for simulated data. Signal values along  $x$ -axis are all above the pedestal. Data counts are shown by color scale.

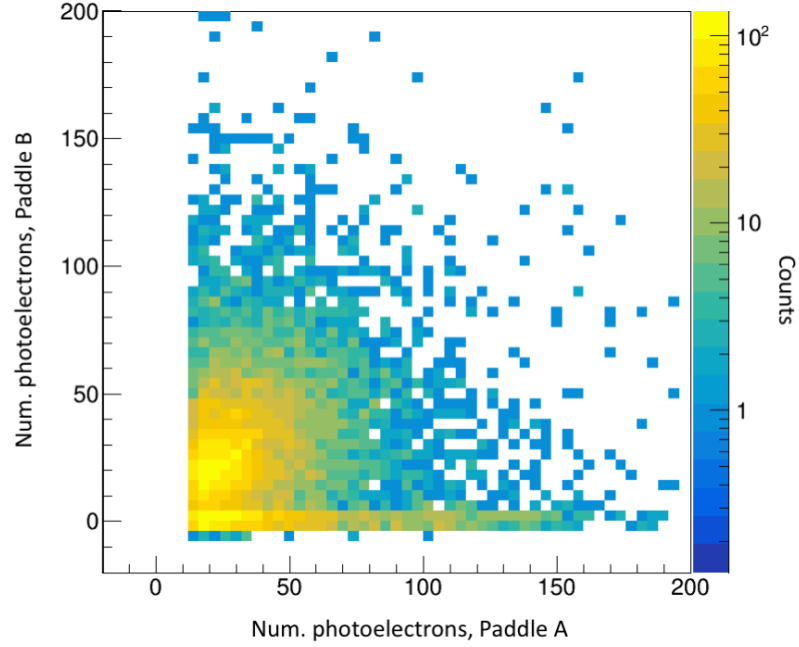


Figure 44: 2-D histogram showing PE signal in one pixel vs. PE signal in adjacent pixel with adjacent paddle for test data. Signal values along  $x$ -axis are all above the pedestal. Data counts are shown by color scale.

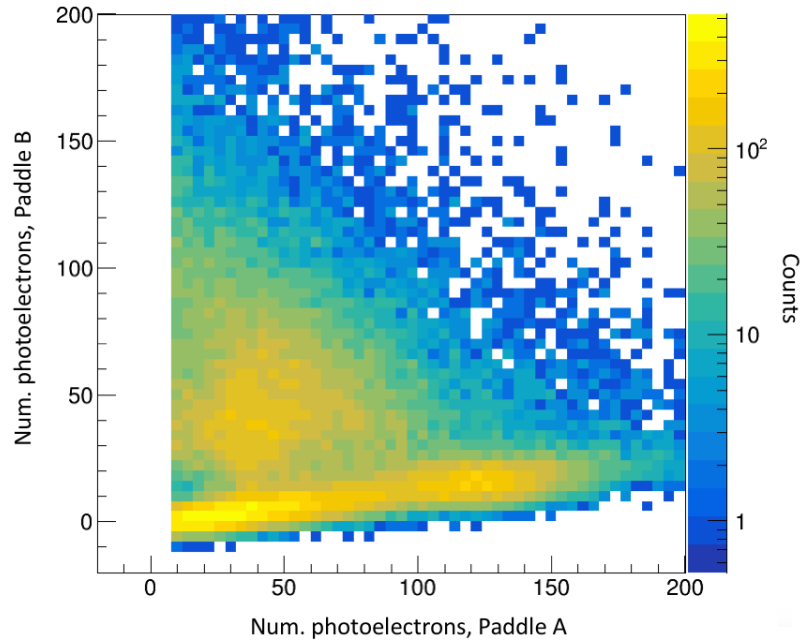


Figure 45: 2-D histogram showing PE signal in one paddle vs. PE signal in adjacent paddle for simulated data. Signal values along  $x$ -axis are all above the pedestal. Data counts are shown by color scale.

More signal sharing is observed between adjacent paddles (Figs. 44 and 45). In Fig. 44, the region of shared signals in the lower left corner is significantly larger than in Fig. 42, as expected, because primaries are more likely to pass through both paddles. However, the general behavior is the same. The smaller the signal present in paddle A, the higher the probability that a signal of significant size is also present in paddle B; the larger the signal present in paddle A, the lower the probability that a signal of significant size is present in paddle B. For reasons not studied in detail, signal sharing between neighbor paddles is more prevalent in the simulation (Fig. 45) than in the real data. However, the overall form of the distribution is still the same.

The analysis of the data from PMT 7 (CDet Module 1 right half) supports the expectation that the level of crosstalk is a small percentage of the real signal. According to the plot in Fig. 42, the level of crosstalk in most of the vertical track region is around 10% or less. Considering the distributions in Fig. 37, this “crosstalk” would be in the pedestal region, where it cannot be confused with a real signal.

### **Detection efficiency and experimental threshold**

Based on the vertical track distributions of photoelectron number (see Fig. 37), the appropriate experimental threshold for CDet is estimated to be around 20 photoelectrons. This will ensure that the whole pedestal is cut out while accepting all relevant signals.

To verify the detection efficiency of CDet at this threshold, the threshold value must be converted from PE number to energy deposited in order to compare it with the results from the old design-phase simulation of CDet [16]. The conversion is simple:

$$\text{Energy threshold} = \frac{(\text{PE threshold})}{\langle PE \rangle} \times \langle E_{\text{dep}} \rangle, \quad (18)$$



where  $\langle PE \rangle$  is the average mean photoelectron number from Eq. 15 and  $\langle E_{dep} \rangle$  is the average mean energy deposition from Eq. 16. Therefore,

$$\text{Threshold (MeV)} = \frac{20}{117} \times 7.24 \text{ MeV} = 1.24 \text{ MeV} \quad (19)$$

Referring back to Fig. 13 in Chapter II, the detection efficiency at this threshold is around 99%. This is the optimal detection efficiency for CDet.

In order to be used in the real CDet data acquisition system, the threshold value of 20 photoelectrons will need to be converted into more appropriate units. The necessary conversion parameters will include the gain on the maPMTs, the electron charge, and any relevant parameters on the NINO cards.

## CHAPTER V: CONCLUSIONS

The CDet bar simulation has been successfully used to calibrate the CDet ADC spectra. The correct parameters have been found to compute the proportionality between ADC channel and energy deposition in the scintillator for each pixel in the detector. The proportionality constant was found to be given by

$$C = \frac{(7.24 \pm 0.12) \text{ MeV}}{\langle \text{ADC} \rangle}, \quad (20)$$

where  $C$  is the proportionality constant in units of MeV per ADC channel and  $\langle \text{ADC} \rangle$  is the mean ADC channel in the vertical track peak from one pixel.

The proportionality,  $P$ , of photoelectron yield to energy deposited in CDet, per pixel, was found to be

$$P = (16.2 \pm 0.28) \text{ PE/MeV}. \quad (21)$$

The simulation was also successfully used to test aspects of the performance of CDet. The level of crosstalk between pixels in maPMT 7 in Module 1 (right half) was found to be small. It is safe to assume that significant crosstalk is not a concern for this maPMT.

The optical efficiency of a single CDet bar was found to be good. The mirror on the inner end of the bar significantly improves the signal. The dependence of the signal on the incident primary position along the bar is less than 0.4 %/cm.

The detection efficiency of CDet was found to be about 99%. The appropriate experimental threshold was determined to be about 20 photoelectrons.

These results will be communicated to appropriate members of the SBS collaboration. The ADC calibration formula will support the commissioning of CDet.

The proportionality of photoelectron yield to energy deposition will be used by the SBS simulation group with their model of CDet. This will aid in the testing and commissioning of the entire spectrometer. The determined experimental threshold will be used in the CDet data acquisition system.

## REFERENCES

- [1] C. Keppel. *The Particle/Nuclear Interface - I*. Presentation slides. Lecture at CTEQ Summer School. July 2017. URL: <http://www.physics.smu.edu/olness/ftp/misc2/cteq/2017/keppel.pdf>.
- [2] X. Ji. *Probing the Internal Structure of the Proton*. PDF. Lecture notes. URL: <http://physics.umd.edu/courses/Phys741/xji/chapter4.pdf>.
- [3] Jefferson Lab website. URL: <https://www.jlab.org>.
- [4] “cebaf.png”. PNG image. URL: <http://inspirehep.net/record/1514923/files/cebaf.png>.
- [5] JLab Hall A info page. URL: <https://www.jlab.org/research/hall-a>.
- [6] SBS homepage. URL: <https://hallaweb.jlab.org/12GeV/SuperBigBite/>.
- [7] *The Super BigBite project: physics and optimization*. Presentation slides. URL: [http://people.virginia.edu/~gdc4k/sbs/sbs\\_phys\\_and\\_optimization\\_w\\_v1.pdf](http://people.virginia.edu/~gdc4k/sbs/sbs_phys_and_optimization_w_v1.pdf).
- [8] C. W. de Jager *et al.* *The Super-Bigbite Spectrometer for Jefferson Lab Hall A*. Jan. 20, 2010, pp. 1–2. URL: [https://userweb.jlab.org/~mahbub/HallA/SBS/SBS-CDR\\_New.pdf](https://userweb.jlab.org/~mahbub/HallA/SBS/SBS-CDR_New.pdf).
- [9] A. J. Sarty. *JLab Internal Design Review: Scintillator-based Coordinate Detector*. Presentation slides. Feb. 25, 2014. URL: <https://hallaweb.jlab.org/wiki/images/c/c2/CDet-Internal-Review-Feb2014.pptx.pdf>.
- [10] CDet on SBS Wiki. URL: [https://hallaweb.jlab.org/wiki/index.php/SuperBigBite#Coordinate\\_Detector](https://hallaweb.jlab.org/wiki/index.php/SuperBigBite#Coordinate_Detector).
- [11] *Photomultiplier Tubes: Basics and Applications*. Edition 3a. Hamamatsu Photonics K. K., 2007, pp. 13, 170–171. URL: [https://www.hamamatsu.com/resources/pdf/etd/PMT\\_handbook\\_v3aE.pdf](https://www.hamamatsu.com/resources/pdf/etd/PMT_handbook_v3aE.pdf).
- [12] M. Novak. *Detector Simulation*. Presentation slides. Slides 5-9. CERN Summer Student Program lecture. CERN, Aug. 1, 2017. URL: [https://indico.cern.ch/event/634284/attachments/1476341/2337717/detector\\_simulation\\_lecture\\_2017.pdf](https://indico.cern.ch/event/634284/attachments/1476341/2337717/detector_simulation_lecture_2017.pdf).
- [13] V. D. Elvira. *Impact of Detector Simulation in Particle Physics Collider Experiments*. Fermi National Accelerator Laboratory, June 15, 2017, pp. 1–3. DOI: 10.1016/j.physrep.2017.06.002. arXiv: 1706.04293 [hep-ex].
- [14] Geant4 website. URL: <http://geant4.web.cern.ch>.

- [15] *Introduction to Geant4*. Geant4 Collaboration. 2018. URL: <http://geant4-userdoc.web.cern.ch/geant4-userdoc/UsersGuides/IntroductionToGeant4/html/IntroductionToG4.html>.
- [16] L. Pentchev and B. Wojtsekhowski. *The concept and main characteristics of the PMT-based Coordinate Detector*. Draft version. Jan. 11, 2014. URL: [https://userweb.jlab.org/~bogdanw/CDet\\_V3.pdf](https://userweb.jlab.org/~bogdanw/CDet_V3.pdf).
- [17] M. Khandaker *et al.* *Coordinate Detector Conceptual Design*. Aug. 16, 2012. URL: [https://userweb.jlab.org/~jones/SBS/CDreport\\_dir\\_aug15/CDreport.pdf](https://userweb.jlab.org/~jones/SBS/CDreport_dir_aug15/CDreport.pdf).
- [18] R. Dollan. *Simulation of optical processes in GEANT4*. Presentation slides. DESY – Zeuthen, Feb. 24, 2005. URL: [https://www-zeuthen.desy.de/lcdet/Feb\\_05\\_WS/talks/rd\\_lcdet\\_sim.pdf](https://www-zeuthen.desy.de/lcdet/Feb_05_WS/talks/rd_lcdet_sim.pdf).
- [19] *Plastic Scintillating Fibers*. PDF. Saint-Gobain Crystals. URL: <https://www.crystals.saint-gobain.com/sites/imdf.crystals.com/files/documents/fiber-product-sheet.pdf>.
- [20] A. Sarty. *Multi-anode Photomultiplier Tube Performance Assessment Tests for Jefferson Lab*. Presentation slides. Oct. 30, 2013. URL: <https://hallaweb.jlab.org/12GeV/SuperBigBite/SBS-minutes/2013/CDet-PMT-testingResults-30Jan2013.pptx.pdf>.
- [21] *User’s Guide for Application Developers*. Rev. 3.1. Section “How to Define a Detector Geometry”. Geant4 Collaboration, 2018. URL: <http://geant4-userdoc.web.cern.ch/geant4-userdoc/UsersGuides/ForApplicationDeveloper/html/index.html>.
- [22] P. Gumplinger. *Optical Photon Processes in GEANT4*. Lecture notes. Presented by J. Apostolakis at CERN Users’ Workshop. TRIUMF/GEANT4, 2002.
- [23] A. Schälicke. *Optical Physics*. Presentation slides. Geant4 tutorial. Material adapted from P. Gumplinger and G. Santin. DESY, Zeuthen, Feb. 18, 2010. URL: <https://indico.cern.ch/event/58317/contributions/2047457/attachments/992304/1411067/OpticalPhysics.pdf>.
- [24] *Physics Reference Manual Documentation*. Release 10.3. Geant4 Collaboration, Sept. 27, 2017, pp. 155–156, 159. URL: <https://indico.cern.ch/event/647154/contributions/2714212/attachments/1529029/2397030/PhysicsReferenceManual.pdf>.
- [25] ROOT website. CERN. 2018. URL: <https://root.cern.ch>.
- [26] ROOT - About page. CERN. 2018. URL: <https://root.cern.ch/about-root>.

- [27] P. Shukla and S. Sankrith. *Energy and angular distributions of atmospheric muons at the Earth*. Oct. 1, 2018, pp. 5–7. arXiv: 1606.06907v3 [hep-ph].
- [28] *Birks' law*. URL: [https://en.wikipedia.org/wiki/Birks%27\\_law](https://en.wikipedia.org/wiki/Birks%27_law).
- [29] M. Tanabashi *et al.* (Particle Data Group). Phys. Rev. D 98, 030001 (2018). DOI: <https://doi.org/10.1103/PhysRevD.98.030001>.
- [30] I. S. Jones. *The energy loss of relativistic cosmic ray muons in plastic scintillator*. Fig. 2.5. Master's thesis. (1969) Durham University. Available at Durham E-Theses Online. URL: <http://etheses.dur.ac.uk/10163/>.

